coatings

MDPI

Article

The Effect of Laser Shock Peening (LSP) on the Surface Roughness and Fatigue Behavior of Additively Manufactured Ti-6Al-4V Alloy

Krista Dyer [1], Samira Ghadar [1], Sanin Zulić [2], Danijela Rostohar [3], Ebrahim Asadi [1,†] and Reza Molaei [1,*]

[1] Department of Mechanical Engineering, The University of Memphis, Memphis, TN 38152, USA
[2] HiLASE Centre, Institute of Physics of the Czech Academy of Sciences, 25241 Dolní Břežany, Czech Republic
[3] Institute for Advanced Manufacturing and Engineering, Coventry University, Coventry CV6 5LZ, UK
* Correspondence: rmolaei@memphis.edu
† Current Organization: Medtronic Plc, Memphis, TN 38120, USA.

Abstract: Laser shock peening (LSP) uses plasma shock waves to induce compressive residual stress at the surface of a component which has the potential to improve its fatigue properties. For AM parts, the existence of internal defects, surface roughness, and tensile residual stresses leads to noticeably lower fatigue strength compared to materials produced through conventional processes. Furthermore, there is a tendency for greater scatter in the fatigue behavior of these parts when compared to traditionally manufactured components. In this study, the effect of LSP on the roughness and fatigue behavior of Ti-6Al-4V alloy constructed through Laser Powder Bed Fusion (L-PBF) technique was investigated. Two types of samples were designed and tested: as-built surface air foil samples for four-point bending tests and machined surface straight gage samples for uniaxial fatigue testing. Two sets of process parameters, optimized and non-optimized, were also used for the fabrication of each sample type. It was found that LSP had negative effects on the smooth (i.e., machined) surface samples, whereas for as-built surfaces the roughness was enhanced by decreasing the sharpness of the deep valleys and partially remelting the loosely bonded particles on the peaks. It was found that the scatter of the fatigue data decreased for optimized machined samples, while no clear improvement was observed in their lives. However, all non-optimized samples showed improvements in fatigue lives after the LSP process.

Keywords: additive manufacturing; laser shock peening; fatigue; surface finish; roughness

Citation: Dyer, K.; Ghadar, S.; Zulić, S.; Rostohar, D.; Asadi, E.; Molaei, R. The Effect of Laser Shock Peening (LSP) on the Surface Roughness and Fatigue Behavior of Additively Manufactured Ti-6Al-4V Alloy. *Coatings* **2024**, *14*, 110. https://doi.org/10.3390/coatings14010110

Academic Editor: Jinyang Xu

Received: 17 December 2023
Revised: 9 January 2024
Accepted: 9 January 2024
Published: 15 January 2024

1. Introduction

Additive Manufacturing (AM) is an innovative technology that constructs parts through a layer-by-layer addition of material. In general, AM consists of using an energy source such as a laser or electron beam to melt layers of powder or wire metal into a specified geometry. There are two main types of AM processes, Powder Bed Fusion (PBF) and Directed Energy Deposition (DED). In PBF, the powdered material is first spread across a build plate and then melted selectively into the desired shape. This process is repeated until the part is fully formed. On the other hand, DED creates layers by simultaneously depositing and melting the material onto the build plate. This method can have higher geometric inaccuracies compared to PBF [1].

AM has a variety of benefits over traditional subtractive methods that have caused it to gain attention in many industries. One of the most significant advantages is the ability to fabricate complex geometries with limited time, cost, and material waste. Because of the layered nature of AM, geometries that would have been extremely challenging, if not impossible, to build through subtractive techniques can be made with relative ease [2]. This has applications ranging from the easier customization of parts in the biomedical field to the production of lightweight components in the aerospace industry. Furthermore, with

the appropriate machinery and materials, AM also allows for rapid prototyping and onsite manufacturing of these application specific components [3]. AM continues to progress in terms of materials and technologies providing increasing potential for development in various industries.

Despite these advantages, AM has been slow to integrate into wide scale production due to some ongoing challenges. Some of these include defects, surface roughness, build orientation, and residual stresses. All of these factors can have drastic impacts on the mechanical behavior of the part; thus, the variability in the factors can cause inconsistencies in their properties. Many AM components undergo cyclic loading conditions, exposing them to the potential for fatigue failures [4]. Understanding the fatigue behavior of AM components is important so that the full range of applications can be used safely.

The melting and re-solidification processes necessary for melting-based AM processes naturally induce a range of defects in the form of un-melted powder, called Lack of Fusion (LOF) defects, or entrapped gas pores throughout the final component. LOF defects are small irregularly shaped sections of un-melted powder that can cause significant stress concentrations within the structure [1,5]. Insufficient heating is just one of the many potential causes for these defects. On the other hand, spherical gas pores, also called voids, form within the melt pool. However, there are different types of void defects that can be more harmful to fatigue performance than others. For example, keyhole porosities stay at the surface of the melt pool and become trapped by the subsequent layers of material, resulting in irregularly shaped voids that have higher stress concentrations than their more uniform counterpart [6].

In Laser Powder Bed Fusion (L-PBF), the formation of these defects can be largely affected by the energy transferred from the laser to the powder. One of the many ways to optimize the energy input for improved part quality is through a factor called energy density (E). This value represents the relationship between some of the major process parameters as shown below:

$$E = \frac{P}{vht} \tag{1}$$

where P is the laser power, v is the laser scan speed, h is the hatch spacing, and t is the layer thickness [7].

Although there are recommended E values for different applications, there is not a single E value that can result in the highest density for every geometry, and determining that ideal energy density value can take extensive testing. However, energy density is just one of the hundreds of parameters that can impact the quality of a part, making the effect of varying process parameters a continued obstacle in AM.

In addition to the impact of process parameters, surface roughness can significantly lower the component's fatigue life. Rough surfaces present pre-formed initiation sites for fatigue cracks that can quickly progress to full fracture. In many AM geometries it is impractical, if not impossible, to reduce the surface roughness through machining or polishing, hence it is vital to understand the effect of as-built AM surfaces on the mechanical properties and how different factors can influence the surface conditions [8]. For example, build orientation can affect surface roughness and, in turn, fatigue performance. The angle and direction in which a part is constructed can cause discontinuity between layers on the surface, called the stair stepping effect. This phenomenon is commonly seen in instances of curved or angled surfaces and directly increases the surface roughness [9].

The repeated heating and cooling of AM processes cause temperature gradients between layers which often can result in significant internal residual stresses within the final component. During the PBF process, an abrupt temperature gradient forms within the structure as a result of the quick heating as well as the relatively slow heat dissipation. Since the bottom layers prevent the heated top layers from expanding, it can cause elastic compressive strains. The top layer will be plastically compressed when the material's yield strength is reached, which is lowered at high temperatures. The plastically compressed upper layers begin to shrink and bend in the direction of the laser beam after cooling which

leaves residual stresses [10,11]. This stress can become a significant portion of the yield strength, causing failures to occur at lower applied stresses than anticipated. Residual stress can be either tensile or compressive, which results in detrimental or beneficial effects on the material properties. For instance, tensile residual stresses encourage crack opening that can eventually lead to failure. On the other hand, compressive residual stresses can counteract the applied tensile stresses, resulting in the experienced stresses being lower than what was applied nominally. Post manufacture treatment methods such as annealing have been developed to relax the residual stresses by heating a part and slowly cooling it to remove the temperature gradients [12].

Laser Shock Peening

A process called Laser Shock Peening (LSP) induces compressive residual stresses, to potentially combat some challenges present with AM. LSP uses plasma-induced shock-waves which travel below the surface of the target body to cause slight plastic deformation as shown in Figure 1. The laser beam vaporizes an opaque layer (typically Vinyl tape) which produces plasma along the target surface. The opaque layer is meant to serve as a small barrier to preserve the surface quality of the work piece. The transparent layer will ensure safe energy transfer from the plasma to shock waves by preventing the expansion of created plasma [13]. The plastic deformation causes compressive residual stresses at the surface and tensile residual stresses in the interior regions (i.e., within the volume) to satisfy equilibrium throughout the component [14]. Because most fatigue cracks form at or near the surface, these compressive residual stresses have the potential to slow their formation and, in turn, improve the fatigue lives in some applications. LSP has been studied for a variety of applications and materials. Pathak et al. [15] studied the effectiveness of LSP on 304L stainless steel alloy with and without surface finishing and heat treatments. The residual stresses were measured before and after LSP for four different conditions including: As-Built (AB), AB + annealed, AB + polished, and AB + annealed + polished. The results indicated that LSP was effective in all cases of heat treatments and surface conditions while it induced the most compressive residual stresses for the case of AB + annealed + polished samples at 0.1 mm depth. It was consistent in all cases that the highest compressive residual stresses did not occur at the surface, but at depths around 0.1 mm below the surface [15].

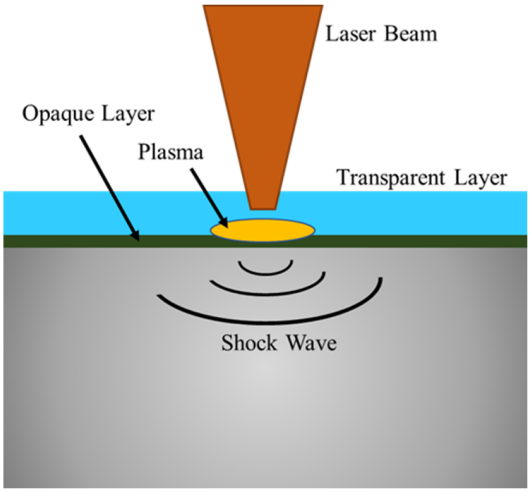

Figure 1. Schematic of laser shock peening process.

Another study examined the LSP process on the tensile properties of 316L stainless steel with different build directions [16]. Tensile samples were fabricated using selective laser melting at 0, 45, and 90-degree orientations, and all were tested with polished surface conditions. LSP converted the tensile residual stresses at the surface of all as-built (no stress relieved) samples to compressive residual stresses, with the most prominent case being the 45-degree samples at a value of −628 MPa. Additionally, the tensile properties

were impacted by the LSP process. The ultimate tensile strength increased by 4%, 3.5% and 7% for the 0, 45, and 90-degree samples, respectively. Lastly, the 0 and 90-degree specimens experienced lower percent elongation. This was found to contradict the behavior of traditionally manufactured 316L parts, where the elongation is known to increase after the application of LSP [16]. While LSP affects the behavior of materials, coupling it with the vast possibilities of AM processes can result in further variations in their properties.

There have been some studies investigating the effect of LSP coupled with other factors such as surface roughness and fatigue behaviors. Aguado-Montero et al. [17] discussed the effect of different surface treatments on the fatigue strength of a sand-blasted and annealed AM Ti-6Al-4V alloy. These treatments included shot peening, laser peening, and a combination of shot peening and chemical-assisted surface enhancement. It was concluded that LSP did not cause significant changes to the surface roughness, while it generated residual stress distributions with slightly lower peaks, compared to shot peening. This was discussed to be the reason for the highest fatigue strength of LSP samples among the three analyzed treatments. It was also concluded that the location of all failures caused by interior cracks were below the compressive residual stress regions where the cyclic loads induced the highest stress intensity factors.

A similar study [18] also addressed the effect of multiple surface post-processing procedures on an as-built surface Ti-6Al-4V alloy produced with both L-PBF and Electron Beam Powder Bed Fusion (E-PBF). The surface processing methods included shot peening, laser shock peening, centrifugal finishing, laser polishing, and linishing. The study concluded that for all five methods, L-PBF samples exhibited higher fatigue limits as compared to E-PBF parts, which was attributed to the finer as-built surface roughness of L-PBF samples. The surface roughness for L-PBF samples, before and after LSP, was reported to be about 15 µm in terms of S_a. They mentioned that surface roughness alone could not adequately predict fatigue properties for surface post-processed material. This was because any prior surface defects, or microstructural changes, could be hidden beneath a smooth surface. A noticeable (about 23.6%) increase in the fatigue strength of the TC17 titanium alloy was observed after LSP as compared to the as-built condition. Similarly, Yang et al. [19] showed that the fatigue life of Ti-6Al-4V notched specimens was enhanced by about 2.5 times in the High-Cycle Fatigue (HCF) regime after undergoing the LSP processes. They also concluded that the interaction between the LSP treatment and the notch influenced the initiation location of fatigue cracks competitively. The study stated that although there was a significant difference in stress distribution between the surface and interior regions of the specimens, fatigue cracks still tended to initiate from the surface even when the LSP treatment was applied.

While studies in the literature consider the effect of LSP on AM samples with various surface conditions, the effect of LSP on the machined surface condition still needs further investigation. The objective of this study is to address the current gaps in the literature by investigating the effects of LSP on the surface roughness and, subsequently, fatigue properties of as-built and machined surfaces of AM Ti-6Al-4V alloy. In addition, the effect of AM process parameters and the induced volumetric and surface defects are studied to highlight the effectiveness of LSP in improving the fatigue behavior of AM parts when the build process parameters deviate from the optimized values.

2. Experimental Program

2.1. Materials and Sample Preparation

All samples were built from gas atomized Ti-6Al-4V alloy powder with a size range of 15–45 µm using an EOS M290 L-PBF machine. Each sample was manufactured using one of two sets of process parameters listed in Table 1. PBF1 process parameters were recommended by the manufacturer to produce the densest specimens and may be referred to as optimized process parameters. PBF2 process parameters were specifically chosen to slightly deviate from manufacturer's suggested parameters to induce defects. These non-optimized process parameters have a lower energy density than PBF1, generated by

decreasing laser power and laser speed. The new energy density should cause an increase in lack of fusion defects that would have a more noticeable effect on mechanical behavior compared to void defects. As a result, the effect of LSP with the presence of significant defects can be analyzed.

Table 1. Process parameters used in fabrication of the fatigue test specimens.

Parameter Set ID	P (W)	v (mm/s)	h (mm)	t (µm)	Energy Density (J/mm^3)
PBF1	280	1200	0.14	30	55.56
PBF2	150	1100	0.14	30	32.46

Two types of fatigue tests were conducted in this study, four-point bending and uniaxial, each with their own specimen geometries and specifications. One type which is referred to as an air foil specimen, shown in Figure 2a, was used for the four-point bending fatigue tests. All air foil specimens had as-built surface conditions and were fabricated using both sets of process parameters listed in Table 1, in addition to three different build orientations. Vertical samples were used for fatigue testing, and the two non-vertical samples shown in Figure 2b,c were made as extreme cases for surface roughness analysis. The non-vertical specimens were built at 40-degree angles, clockwise and counterclockwise, which are labeled up and down respectively, from the z-axis along the x-z plane. The samples used for axial loading fatigue tests are referred to as uniaxial samples. All uniaxial samples were machined down to the final geometry shown in Figure 2d from vertically built solid rods. These specimens were fabricated using either PBF1 or PBF2 process parameters. A summary of all sample types is presented in Table 2.

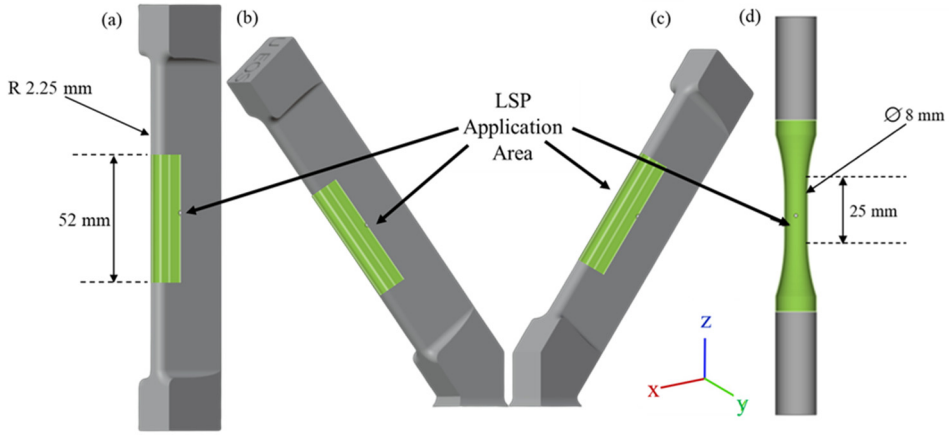

Figure 2. (**a**) Air foil sample geometry for four-point bending fatigue testing. (**b**) Non-vertical angled down air foil sample and (**c**) non-vertical angled up air foil sample geometries for roughness analysis. (**d**) Solid rod sample geometry for uniaxial fatigue testing. LSP regions are highlighted in green.

Table 2. Test specimen types including process ID, surface finish, and build orientation.

Process ID	Sample Type	Surface Finish	Build Orientation
PBF1	Air foil	As-built	Vertical Non-vertical up Non-vertical down
	Uniaxial	Machined	Vertical
PBF2	Air foil	As-built	Vertical Non-vertical up Non-vertical down
	Uniaxial	Machined	Vertical

2.2. Post Processing

In order to have a clear comparison of the effects of LSP on residual stresses, all samples were annealed to relax the initial residual stresses formed during the manufacturing process. The treatment was performed at 700 °C for 2 h based on the results from [20]. Specimens of each type were selected randomly for LSP treatment. The application area for all four geometries is highlighted in Figure 2, and the treatment parameters are reported in Table 3. It is worth mentioning that no opaque layer was used in this work and the plasma was created by melting the surface of the treated samples. The hole drilling method was used with a Stress-tech Prism device in place of a strain gauge to measure the residual stress depth profiles for as-built surface specimens. A drill diameter of 1.65 mm spinning at 40k rpm was used to measure the compressive residual stresses. X-ray Diffraction (XRD) method was utilized to obtain the residual stress depth profiles for machined surface specimens.

Table 3. Laser shock peening process parameters.

Pulse Energy (J)	Laser Source Wavelength (mm)	Pulse Duration (ns)	Pulse Overlapping (%)	Laser Energy Density (GW/cm^2)	Square Spot Size (cm^2)
5	1030	14	50	4.25	0.0841

The surface roughness of uniaxial samples with and without LSP treatment along with the vertical air foil specimens were precisely measured using a Pocket Surf PS1 portable surface profilometer manufactured by Mahr GmbH. This device is equipped with a skidded probe that can measure parameters such as R_a, R_v, R_z, and R_t, and has a measurement range of up to 350 µm for all parameters. The surface roughness values were recorded as the average of five separate measurements within the gage section of each sample. Amongst the different parameters, R_v was used as the basis for measurements and comparisons. It was discussed in [21,22] that this parameter is better capable of capturing the information of the deep valleys that are inherent within the rough surface of AM components. Due to the plastic deformation that LSP imposes on the material surface, the changes in valleys are highly probable. Hence, changes in the R_v values can provide a better understanding of the roughness profile changes caused by LSP compared to other roughness parameters.

In order to further investigate the effect of LSP on surface roughness, an alternative method was also employed for air foil specimens in two different conditions (PBF1 and PBF2). Following the process shown in Figure 3, measurements were conducted on the curved section of the specimens by cutting the center piece of the samples out, followed by a side-to-center thickness polishing. This resulted in 2 mm sections which were used for imaging and roughness profile measurements. A Keyence VHX-7000 optical microscope was then utilized to produce 3 × 8 mm three-dimensional stitched images at 200× magnification. The microscopic images were analyzed using ImageJ software version 1.54d, which enabled the extraction of the surface profile data for each sample. The extracted data was subsequently transferred to Excel for further analysis. The roughness surface was plotted against the length of the specimens, and R_v was measured accordingly.

2.3. Fatigue Tests and Defect Analysis

All fatigue tests were conducted under load-controlled mode with R ratio of 0.1. The air foil samples were tested under four-point bending with a frequency of 85 Hz. The uniaxial tests were conducted on an Instron 8801 servo-hydraulic frame in accordance with ASTM standard E466 [23] and frequencies between 4 and 20 Hz. Following the testing, the fracture surfaces were analyzed using an Optical Microscope (OM).

Defect analyses were conducted on non-LSP PBF1 and PBF2 samples. Each sample was cut within the gage section and polished along the cross section following the related process presented in the Metalog guide [24]. Samples were photographed via the OM and analyzed utilizing ImageJ software version 1.54d. The quantity, maximum size, and percentage of total cross section area for the defects were recorded for discussion.

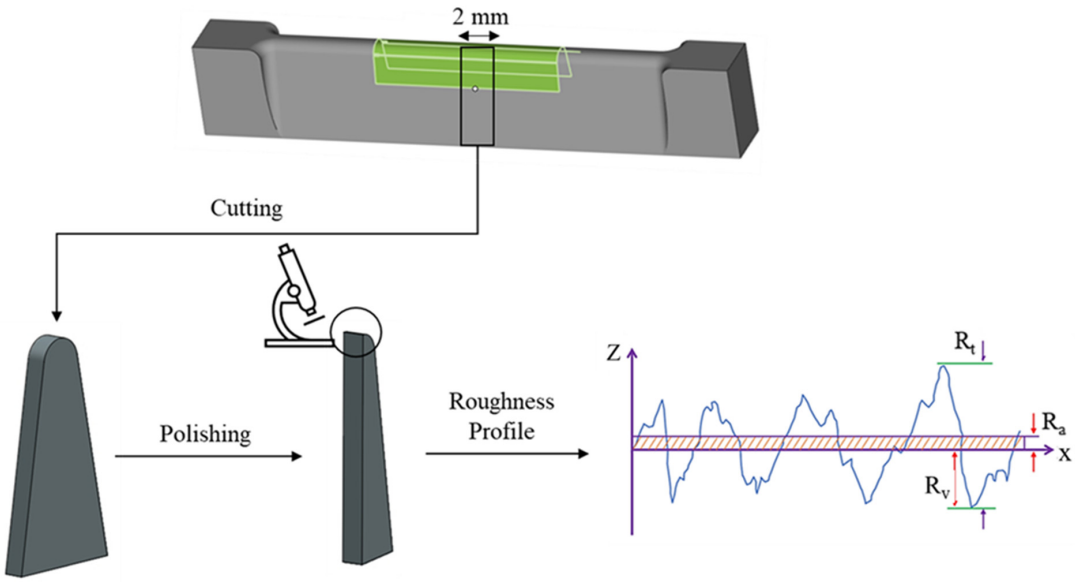

Figure 3. Schematic of sample preparation for roughness measurement on air foil specimens.

3. LSP on As-Built Surface Samples

3.1. Residual Stress

Figure 4 shows the residual stress distributions of the air foil vertical samples with both non-LSP and LSP conditions from 25 to 1000 µm below the surface. Since the surface condition of air foil specimens is as-built, the measurement of residual stress started below the surface to ensure a sufficient distance from any loose powder that might be present on the surface. AM parts generally exhibit tensile residual stresses near the surface due to the solidification process of the molten material and the resulting shrinkage phenomenon inherent to the process. However, annealing relaxed nearly all of the residual stresses created by the AM process and changed it into almost zero for the non-LSP specimens. LSP, on the other hand, results in noticeable compressive residual stresses below the surface with the affected depth of close to 700 µm. These results indicate maximum compressive residual stress values of −320 MPa and −350 MPa located at about 25 µm below the surfaces for PBF1 and PBF2 specimens, respectively. It is worth noting that the difference in compressive residual stresses between PBF1 and PBF2 is not significant.

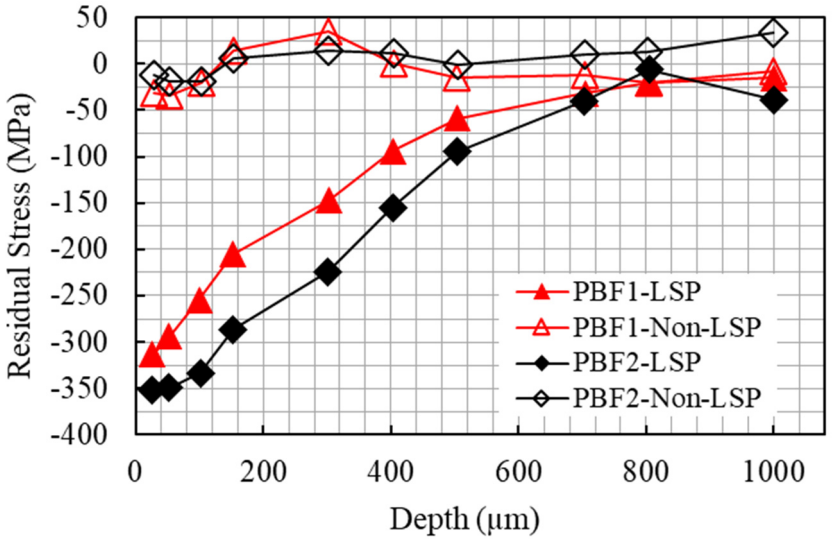

Figure 4. Residual stress depth profile for vertically manufactured as-built surface air foil specimens using hole drilling.

3.2. Surface Roughness

Roughness measurements (R_v) for the four groups of vertical air foil specimens are shown in Figure 5. The roughness data represent the average values obtained from five separate measurements within the gage length of specimens using the Mahr profilometer. Although changes were expected after LSP, the roughness values for both PBF1 and PBF2 samples were similar before and after treatment. A plausible explanation could be the limitations of a mechanical profilometer which may not reach sharp valleys to accurately record roughness details. However, it is worth mentioning that there is a notable difference in surface roughness between PBF1 and PBF2 samples. The process parameters were not optimized for PBF2 samples which induced more unmelted particles on the surface, resulting in increased surface roughness compared to the PBF1.

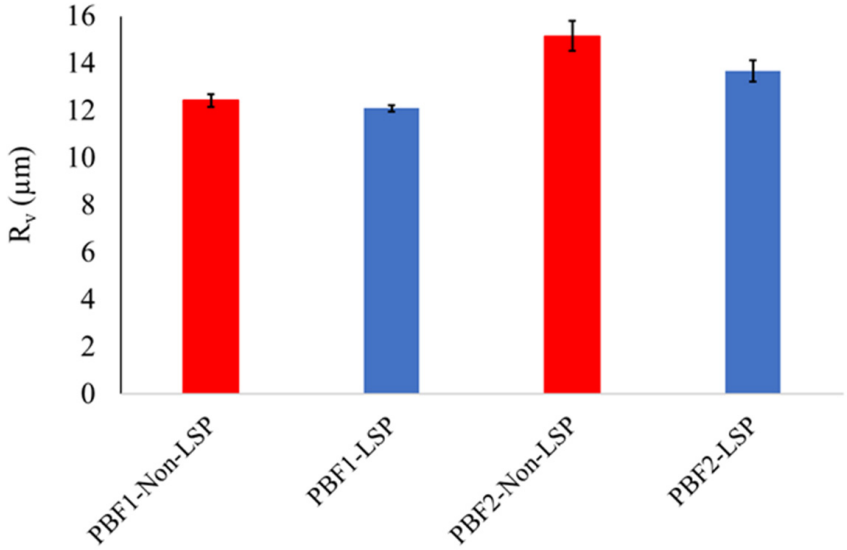

Figure 5. Surface roughness (R_v) of air foil vertical specimens with an as-built surface condition measured with a mechanical profilometer.

While roughness measurements via contact profilometer did not show any significant changes after LSP, a destructive approach was used for further analysis. To do so, in addition to the vertically built samples, two angled samples were built and studied as extreme cases. The non-vertical air foil samples were built with both PBF1 and PBF2 process parameters. These samples were studied due to their significant roughness profiles as compared to the vertical specimens, providing a better basis for the comparison of roughness characteristics before and after the LSP treatment. Roughness measurements were taken on the curved section of the samples, as shown in Figure 3.

Surface roughness measurements (R_v) for all sets of air foil samples using the destructive method are presented in Figure 6. As expected, the measured roughness values for the down-orientated and up oriented specimens are greater than the vertical specimens. This disparity can be attributed to the presence of the stair-stepping effect, which is more pronounced in the non-vertical samples. For the angle specimens, the down-oriented specimens have greater surface roughness compared to the up-orientated specimens. This is most likely due to the addition of overhang with stair-stepping for the down-orientation. This could also be due to the layer-by-layer deposition and greater agglomeration of partially melted feedstock spatters for the non-vertical down specimens [25]. Thus, the build orientation has a significant impact on the surface quality. This result ties well with previous studies where it was found that down-skin specimens have rougher surfaces than up-skin samples [26], and changes in the inclination angle have noticeable effects on the surface roughness [27].

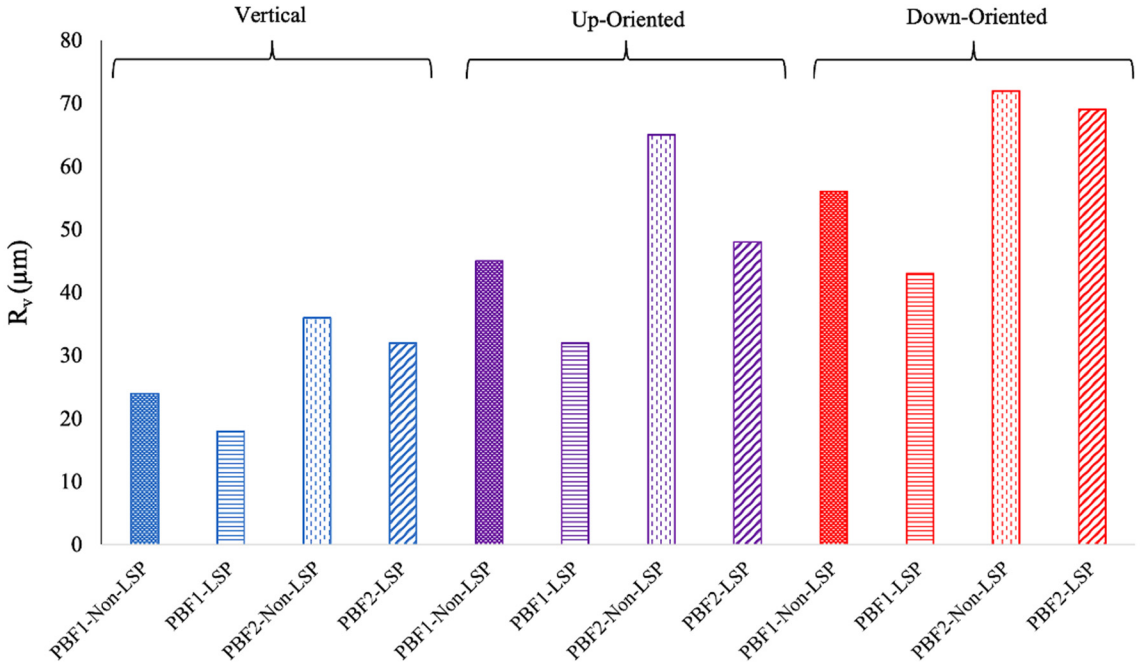

Figure 6. Surface roughness R_v for air foil specimens with an as-built surface finish using the destructive method.

While the profilometer measurements showed no significant effect of LSP on roughness for vertical samples (as shown in Figure 5), the findings presented in Figure 6 demonstrate a notable reduction in surface roughness after LSP for all build orientations. This observation suggests that LSP effectively targets and improves the roughness via the valleys, which may not have been reached using the previous measurement method. The change in surface roughness is most likely due to the melted surface of the part during the LSP process when no opaque layer was used to create the plasma waves, where surface roughness would vary due to differences inherited from the manufacturing process parameters.

A detailed look at the surface texture for the PBF1 non-vertical samples before and after LSP is presented in Figure 7a–d. In parts a and b, numerous unmelted particles above the main surface can be observed before LSP. However, a noticeable reduction in weakly bonded particles can be observed after LSP in parts c and d, resulting in a significant reduction in surface roughness. This observation indicates that LSP has the ability to eliminate loosely bounded particles from the as-built surface, leading to a reduction in roughness. This is consistent with the literature, which suggests that the LSP process can partially remelt and resolidify the unmelted particles of the as-built surfaces [28–31], resulting in a substantial reduction in surface roughness. Consequently, it can be inferred that performing LSP on specimens with an as-built surface can result in the reflowing of the partially melted particles into sharp valleys, and the removal of surface imperfections, which leads to a prominent reduction in surface roughness. While this would generally happen after LSP, the absence of an opaque layer makes it more notable.

Figure 8a, the magnified view of Figure 7b, shows non-uniformly distributed sharp valleys and peaks before the application of LSP. In Figure 8b, which is the magnified view of Figure 7d for the PBF1-LSP condition, the sharpness of the edges is reduced (i.e., blunted), supporting the idea of un-melted or partially melted powder on the surface melting and reflowing into the surface valleys as a result of the LSP process. This is very noticeable in regions IV and V of part b where the sharp valleys are nearly gone. A study by Shen et al. [32] found similar results after LSP, where the sharp protrusions disappeared after LSP treatment. Overall, LSP is effective in significantly altering surface topography, in the form of valley depth, and successfully eliminating imperfections such as spatters and partially melted powders along a surface.

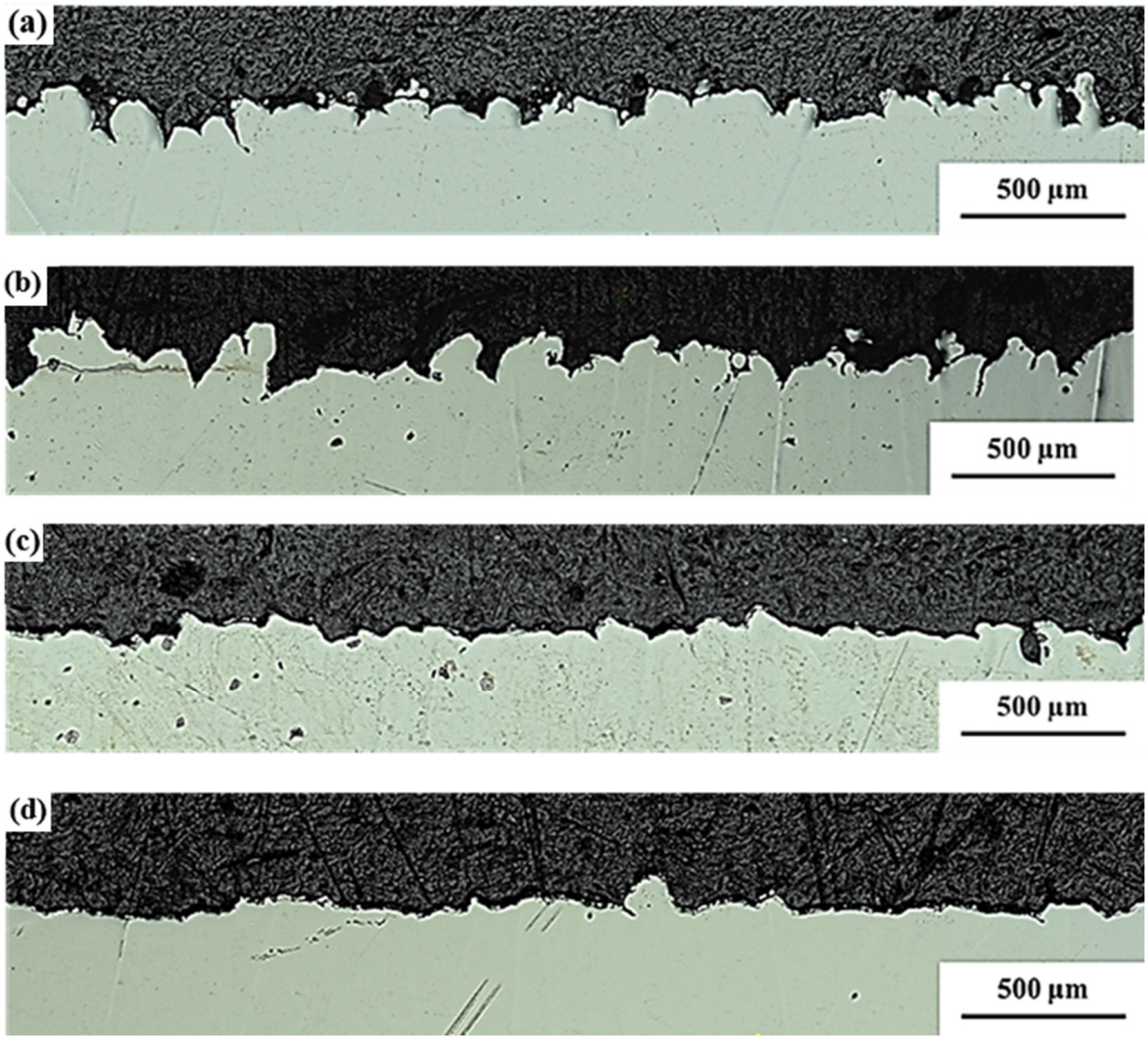

Figure 7. OM images of the (**a**) PBF1 non-LSP-Down, (**b**) PBF1 non-LSP-Up, (**c**) PBF1 LSP-Down, and (**d**) PBF1 LSP-Up.

3.3. Fatigue Test Results and Fractography

Fatigue results for air foil samples are shown in Figure 9. For both PBF1 and PBF2 there is a clear improvement in fatigue strength after LSP for all stress levels tested. The four-point bending fatigue testing method encourages crack initiation from the surface where the highest stress is applied. In samples with high part density and surface roughness, like in the case of PBF1 air foil samples, there are fewer interior stress concentrations to compete with the maximum applied stress on the surface. As a result, all failures initiated from the surface for both LSP and non-LSP PBF1 air foil samples. A selection of fracture surfaces for the PBF1 LSP samples is shown in Figure 10, where each arrow indicates the surface crack initiation. Due to the critical surface locations, the beneficial effects of LSP's compressive residual stresses lower the experienced stress at the surface, causing an improvement in the fatigue life at each stress level. For the higher tested stresses such as 550 MPa, the fatigue life improved by 45,000 cycles for a more than 200% increase, and for the lower stress at 350 MPa, the fatigue life improved to be run out after LSP. This is consistent with the results from [17] which found that LSP caused a large improvement in fatigue life for four-point bending test after annealing and sand blasting.

Apart from the decrease in experienced stress, another contributing factor to the improvement in the fatigue strength of the PBF1 samples is the reduction in surface roughness. Because the surface remained the critical location in all instances of optimized air foil samples, the surface condition likely had a more prominent influence on the fatigue behavior. As discussed in Section 3.2, LSP causes a decrease in the sharpness of the valleys for the as-built surfaces and reduces the unmelted particles remaining on the surface. With fewer sharp valleys, there is less potential for the micro notches to serve as crack initiation. Subsequently, it would take longer for fatigue cracks to form and grow to fracture.

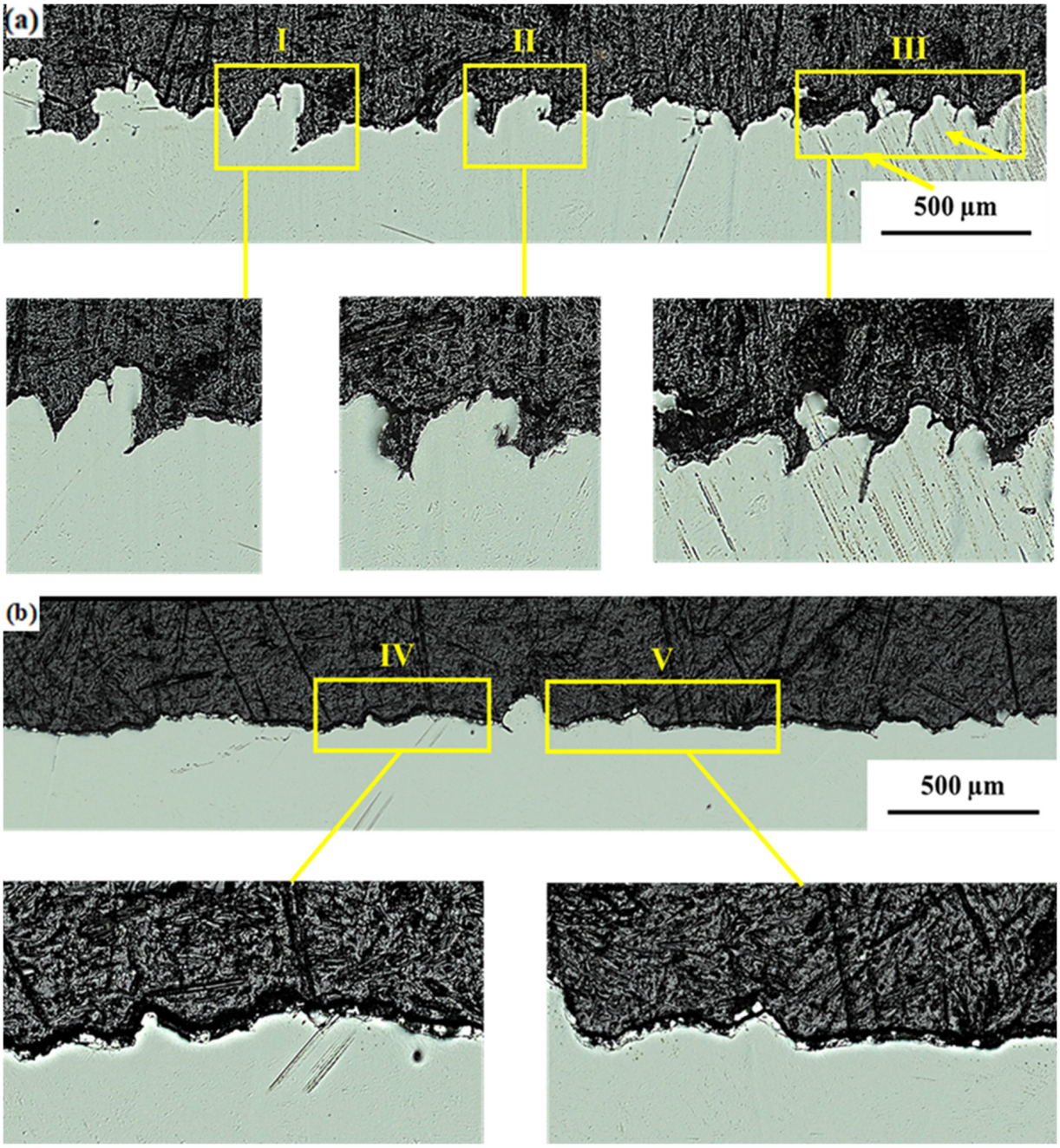

Figure 8. OM images of the (**a**) PBF1 non-LSP-Up, and (**b**) PBF1 LSP-Up. Regions I, II, and III show sharp valleys before LSP and regions IV and V represent the blunt valleys after LSP.

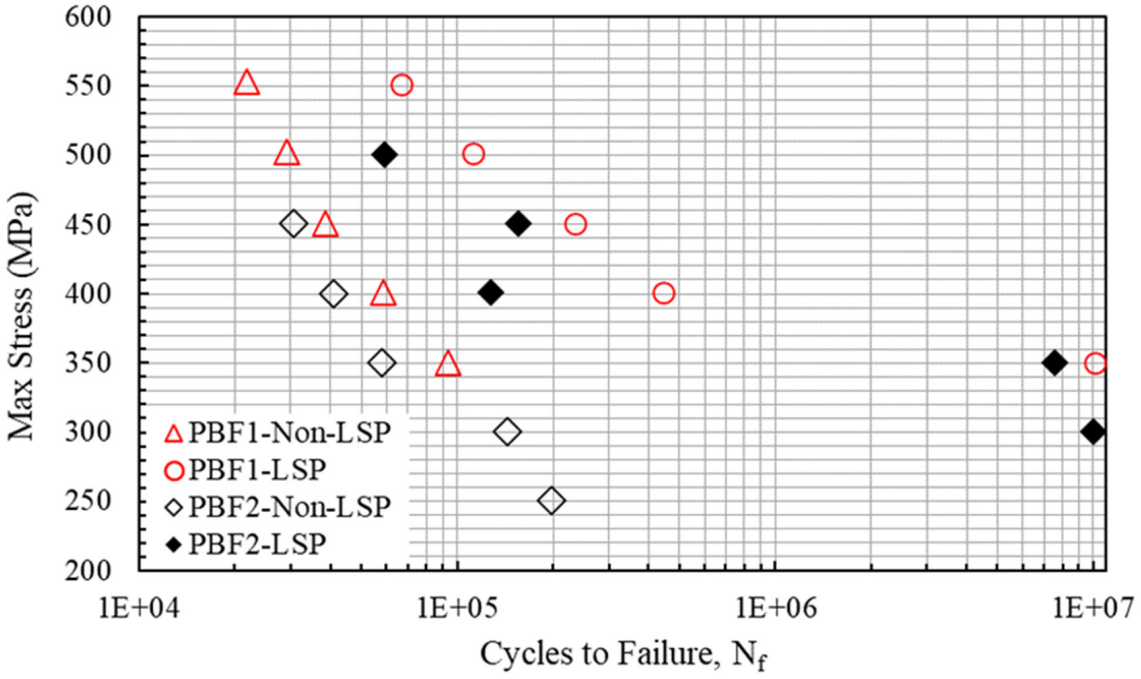

Figure 9. Four-point bending fatigue results for air foil samples.

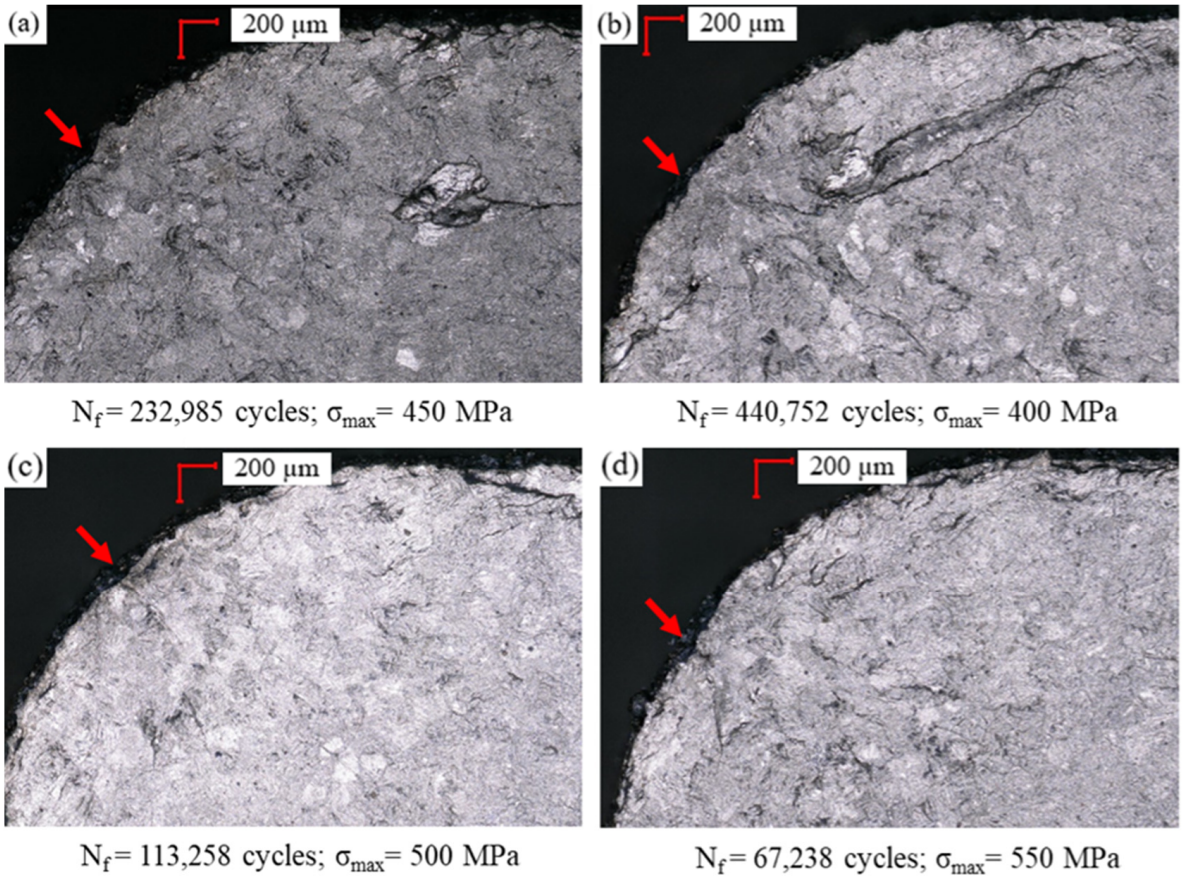

Figure 10. (**a**–**d**) Facture surface images for PBF1 air foil samples subjected to LSP where the red arrows indicate surface crack initiation locations.

A similar trend can be seen for the PBF2 air foil samples. The lives steadily increase as the applied stress decreases, and LSP samples show a much longer life compared to non-LSP

samples at the same stress levels. It is notable that the PBF2 LSP sample tested at 400 MPa failed outside the LSP area, which may account for the deviation from the trend seen by the other data points. Unlike the optimized samples, the crack initiation sites are less consistent for the PBF2 specimens. As presented in Figure 11, failures occurred from both the surface and interior despite the testing method. This is probably the result of increased internal defects with more irregular shapes produced from the different processing parameters. Although some initiations are from the interior, they are still well within the 1000 µm depth, where there is compressive residual stress. Thus, the same crack-closing mechanism of LSP is still present to improve the fatigue life.

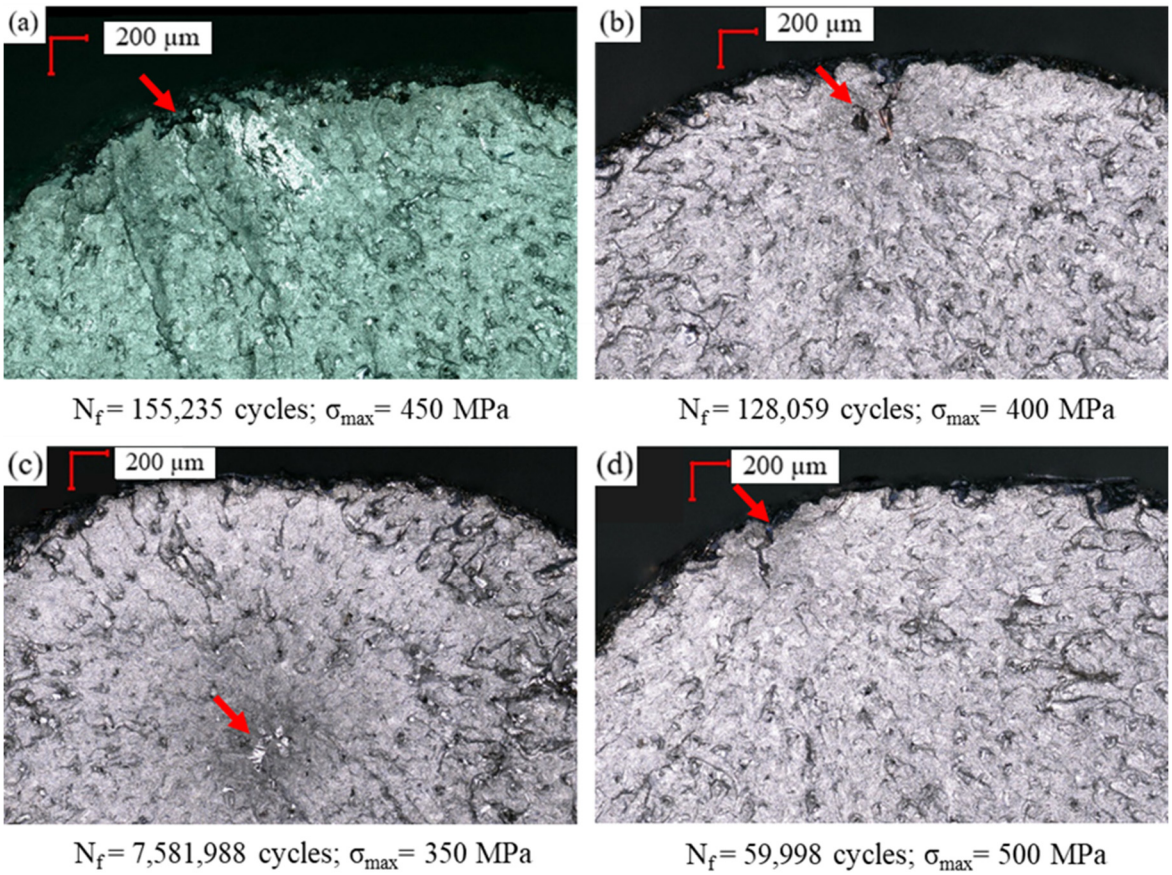

Figure 11. (**a**–**d**) Facture surface images for PBF2 air foil samples subjected to LSP where the red arrows indicate the crack initiation locations.

3.4. Mean Stress Correction Modeling

Residual stresses can significantly impact the experienced stress of a component. Specifically, for LSP components, the compressive residual stresses reduce the magnitude of the stress near the surface. The decrease in maximum and minimum stress results in a different *R* ratio and, thus, mean stress experienced by the component after LSP. Therefore, a mean stress correction method can be applied to account for the change in *R* ratio caused by the compressive residual stresses.

In accordance with the findings presented by Derrick et al. [33], the Smith-Watson-Topper (SWT) method offers a strong correction method for mean stress effects in Ti-6Al-4V. The SWT equation (stress version) which is commonly used to estimate equivalent completely reversed stress amplitude, is presented in Equation (2) where S_e, σ_{max}, and σ_a are fully reversed equivalent stress amplitude, maximum applied stress, and applied stress amplitude, respectively [34].

$$S_e = \sqrt{\sigma_{max}\sigma_a} \quad (2)$$

Given an *R* ratio of 0.1 and known applied stress values, the SWT parameter was easily calculated for the non-LSP data. However, for the LSP samples, the SWT parameter is also influenced by the magnitude of residual stress which is dependent on the depth of the killer defect. Fracture surface optical microscopy images were used to identify the depth of the crack-initiating defect, and the corresponding compressive residual stress at that depth was identified from the residual stress depth profile. The new experienced stress, calculated as the difference between the applied stress and the magnitude of compressive residual stress, and the resultant *R* ratio could then be used to determine the SWT parameter of the LSP samples. The data including initiation depth, compressive residual stress at that depth, and the corrected stress values for each sample are summarized in Tables 4 and 5 for PBF1 and PBF2, respectively.

Table 4. Summary of defect depth, corrected stresses, and life for PBF1 samples with as-built surface.

	Depth (μm)	Residual Stress (MPa)	Nominal Max Stress (MPa)	Corrected Max Stress (MPa)	Corrected Mean Stress (MPa)	N_f (Cycles)	R Ratio
Non-LSP	-	0	553	553	304.2	21,790	0.1
	-	0	503	503	276.6	29,228	0.1
	-	0	451.2	451.2	248.2	38,708	0.1
	-	0	401	401	220.6	58,617	0.1
	-	0	350.4	350.4	192.7	94,015	0.1
LSP	26	−314	551	237.4	−10.6	67,026	−1.1
	26	−314	501	188	−37.8	112,417	−1.4
	26	−314	451	137	−65.7	234,253	−1.96
	26	−314	400.5	87	−93.3	443,558	−3.14

Table 5. Summary of defect depth, corrected stresses, and life for PBF2 samples with as-built surface.

	Depth (μm)	Residual Stress (MPa)	Nominal Max Stress (MPa)	Corrected Max Stress (MPa)	Corrected Mean Stress (MPa)	N_f (Cycles)	R Ratio
Non-LSP	-	0	451	451	247.9	30,760	0.1
	-	0	400	400	220	40,736	0.1
	-	0	350	350	192.7	57,873	0.1
	-	0	300	300	165.1	144,200	0.1
	-	0	251	251	137.9	198,425	0.1
LSP	157	−273	501	228	2.4	58,992	−0.98
	436	−136	401	265	84.6	127,728	−0.36
	26	−352.5	541	98	−104.6	155,681	−3.13

Figure 12 shows the fatigue testing results and corresponding SWT vs. life plots for PBF1 and PBF2 specimens. For both PBF1 (parts a and b) and PBF2 (parts c and d), the results show a strong correlation between non-LSP and LSP data. This implied the capability of the SWT model to reasonably estimate the fatigue life of as-built LSP samples using residual stress measurements, and available non-LSP fatigue sample data.

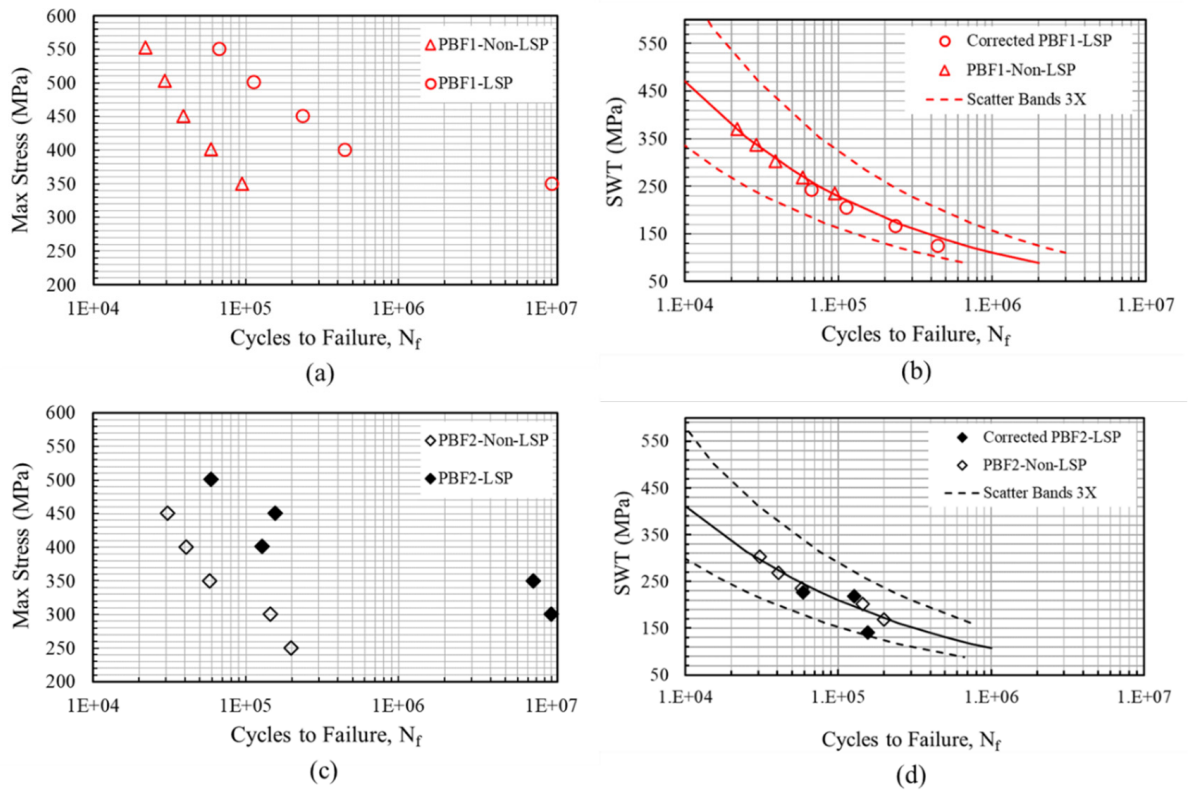

Figure 12. (**a**) Four-point bending fatigue results for PBF1 samples, (**b**) SWT mean stress correction model vs. life for PBF1 samples, (**c**) four-point bending fatigue results for PBF2 samples, and (**d**) SWT mean stress correction model vs. life for PBF2 samples.

4. LSP on Machined Surface Samples

4.1. Residual Stress

The residual stress depth profiles for the uniaxial samples starting from the surface to the depth of about 400 µm below the surface are shown in Figure 13. Because of prior annealing, it was assumed that the residual stresses for non-LSP uniaxial samples were zero. This is supported by the results in Figure 4 which present residual stresses around zero for non-LSP annealed air foil samples. Similar to the air foil samples, residual stresses start in compression near the surface for the LSP samples and gradually increase toward zero. The residual stresses return to zero at a certain depth and start transitioning to tensile. This transition occurs at an approximate depth of 300 µm below the surface, which is much lower than their air foil counterparts. Additionally, the compressive residual stresses at the surface are greater for these samples at maximum values of −600 MPa for PBF1 and −520 MPa for PBF2. As mentioned in Section 3.1, the measurement process for air foil specimens started from a depth of 25 µm below the surface, whereas measurements began directly at the surface for uniaxial samples.

The variations observed in the magnitude and depth of compressive residual stresses between air foil and uniaxial specimens can be attributed to their distinct geometries and surface conditions. LSP targets only a small portion (i.e., volume) of the air foil specimens, while the whole gage section is subjected to LSP for the uniaxial samples, resulting in different responses of the two geometries to the laser wave satisfying equilibrium. As seen in Figure 2, the LSP area for the uniaxial samples completely surrounds the gage section. This causes the equilibrium tensile residual stresses to be limited to the center section of the specimens, which reduces the available volume for the compressive residual stresses. This is not the case for the air foil specimens, where the LSP area is only a small area of the full specimen. As a result, there is more volume and a greater depth of penetration for the compressive residual stresses while maintaining space for the equilibrium tensile residual

stresses in other areas of the component. In addition, the machined surface specimens are smoother and have a smaller number of voids compared to the as-built surface samples. As a result, a greater amount of the energy from the LSP could be absorbed by the machined surface to result in plastic deformation, in contrast to surfaces that have porous and low-density areas near the surface [35].

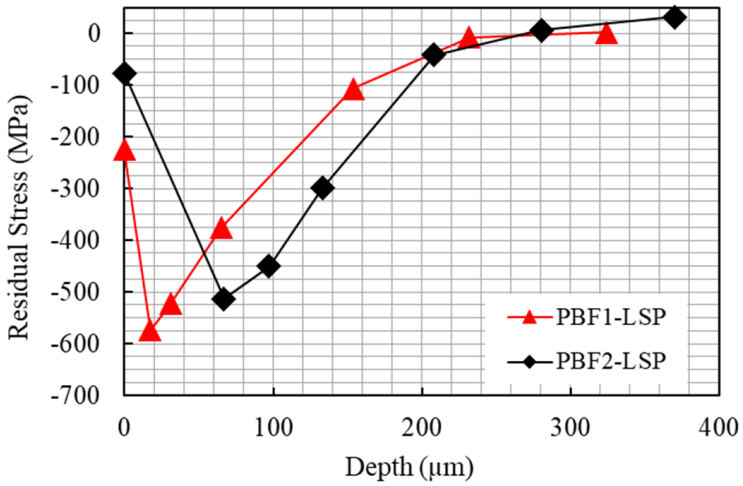

Figure 13. Residual stress depth profile measured via XRD for solid rod machined surface samples subjected to LSP.

4.2. Surface Roughness

The roughness measurement results of the machined surface uniaxial samples obtained by the profilometer are shown in Figure 14. As can be seen, the LSP process increases the surface roughness for both optimized and non-optimized specimens. This indicates that the machined surface specimens are highly sensitive to the LSP process. In other words, unlike the as-built surface samples, the surface roughness can significantly increase when the initial surface is machined and smooth. The nature of the as-built surface condition enables the removal of the partially melted particles and the blunting of the sharp valleys, resulting in a substantial reduction in their roughness. However, this decrease does not occur for the machined surface condition, as there are no sharp valleys to be blunted, and no unmelted particles are present to be melted/removed. Instead, the LSP process introduces new low-profile surface irregularities leading to the increased roughness of the machined surface specimens. As a result, the surface roughness of the machined specimens can be negatively affected by this process.

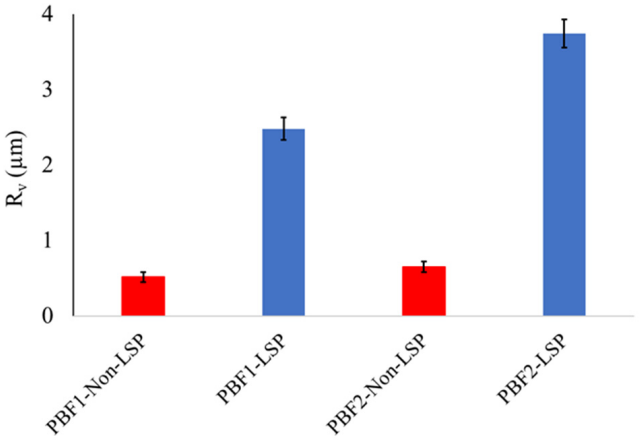

Figure 14. Surface roughness (R_v) of uniaxial specimens with a machined surface condition measured with a mechanical profilometer.

4.3. Fatigue Test Results and Fractography

The fatigue test results for both PBF1 and PBF2 specimens before and after LSP are shown in Figure 15. PBF1 LSP and non-LSP samples were tested with a maximum stress of 700 MPa or 800 MPa. There is not a clear improvement in the fatigue life of the PBF1 LSP samples compared to the untreated samples. Although there is not a clear improvement in fatigue behavior, there is a notable decrease in the scatter for PBF1 LSP results between different trials under the same load. This trend is likely a result of the defect distribution produced from PBF1 process parameters and the adjustment of experienced stress based on the residual stress.

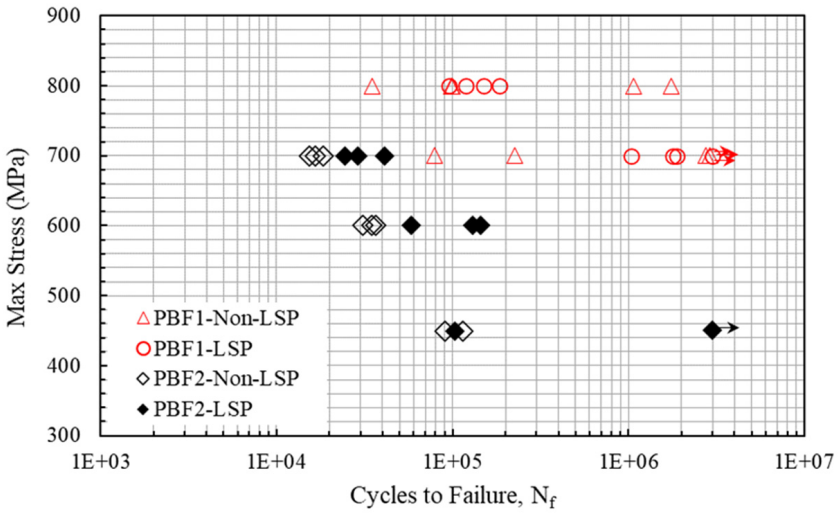

Figure 15. Axial loading fatigue test results for solid rod samples.

PBF1 samples have a limited number of defects which are randomly placed and vary in size between samples. Without being subjected to LSP, the samples may fail from any of the randomized defects within the part. Figure 16 presents the distribution of the crack initiation sites and fatigue lives with their corresponding effective area, based on the Murakami approach [36], for PBF1 samples. A selection of fracture surfaces with the highlighted effective area are shown in Figure 17a–d. Parts a and b outline the measured initial defects for the non-LSP samples while parts c and d indicate a notable pattern at the surface of the LSP samples. This surface texture, resulting from LSP post processing, may act as surface notches for cracks to form. Thus, it is reasonable to approximate the effective area of the surface initiations for LSP samples based on this surface pattern.

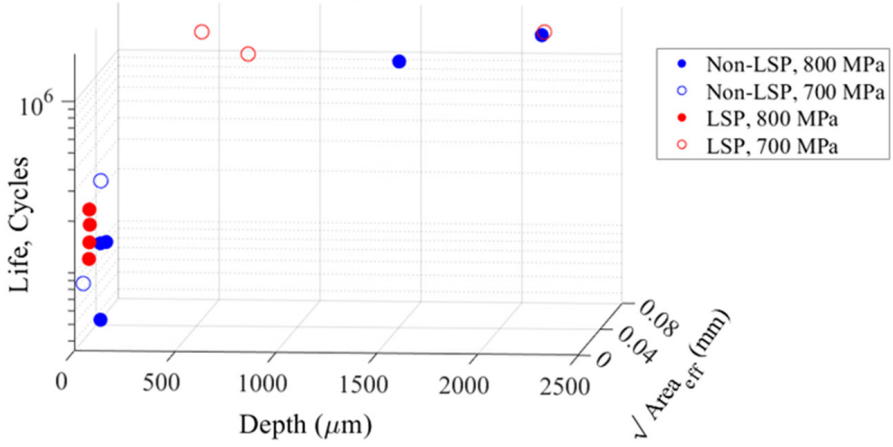

Figure 16. Life, crack-initiating defect depth, and defect effective area for optimized PBF1 uniaxial samples.

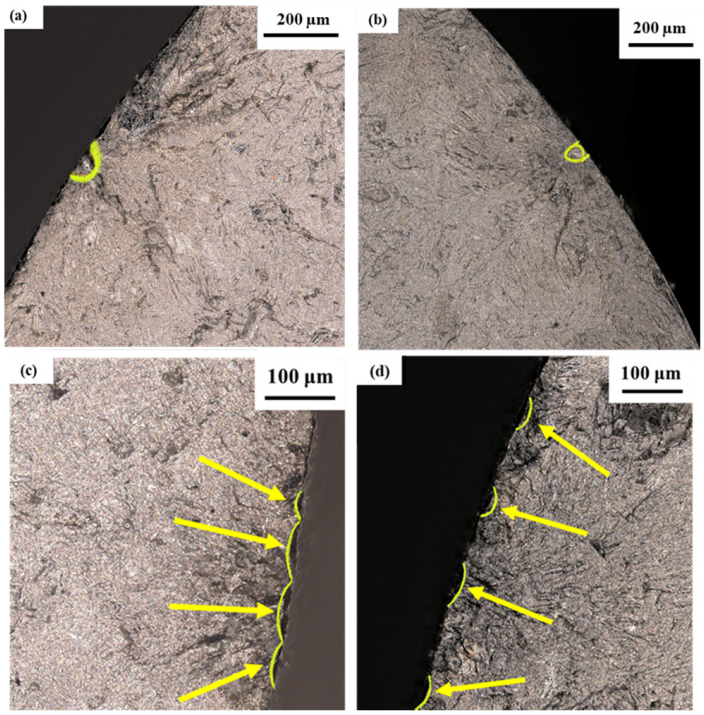

Figure 17. Fracture surfaces for PBF1 (**a**,**b**) non-LSP samples with highlighted crack initiations, and (**c**,**d**) LSP samples with highlighted surface texture pattern.

From Figure 16, the optimized PBF1 samples show a range of initiation sites between the surface and a depth of 2500 µm. However, LSP does not increase the quantity of interior initiation. As discussed in the previous section, LSP has an impact on the surface roughness of a target body along with the compressive stress, which can be either positive or negative depending on the initial surface condition. The surface is already relatively smooth for the machined surface samples, so LSP worsens the condition of the sample by increasing the roughness. The increased surface roughness of LSP samples compared to non-LSP samples would increase the likelihood of crack initiation from the surface and a shorter fatigue life, while the compressive residual stress at the surface from LSP works to decreases the likelihood of crack initiation from the surface and improve fatigue life. The contradicting effects on the fatigue life mean there was minimal increase in internal crack initiations for LSP samples that had the potential to improve the fatigue life.

For more specific instances of Figure 16, Figure 18 highlights three crack initiation locations of PBF1 non-LSP samples under 800 MPa stress. Each initiation site is at a different location along the cross section, and the interior sites differ in the distance from the surface by approximately 750 µm. Crack initiation location plays a notable role in the fatigue life of a part. Significant data have been studied that demonstrate a trend towards longer life for the interior cracks versus surface cracks [37]. Those trends are consistent with the range of locations and corresponding fatigue lives of the PBF1 non-LSP samples. Each of the shown samples was tested under the same stress, however, parts a and b had lives of 1,757,900 and 1,070,031 cycles, respectively, while the life of part c was less than 10% of the others at only 97,996 cycles. A major contributing factor of this variability is most likely the location. The longest life from part a initiates from 2200 µm below the surface, part b initiates at a depth of 1454 µm, and the shortest life initiates from the surface. The lives positively correlate with the initiation distance from the outer surface. As a result, the scatter present in defect initiation locations also presents itself in the range of fatigue lives between the samples which is consistent with the results shown in Figure 16.

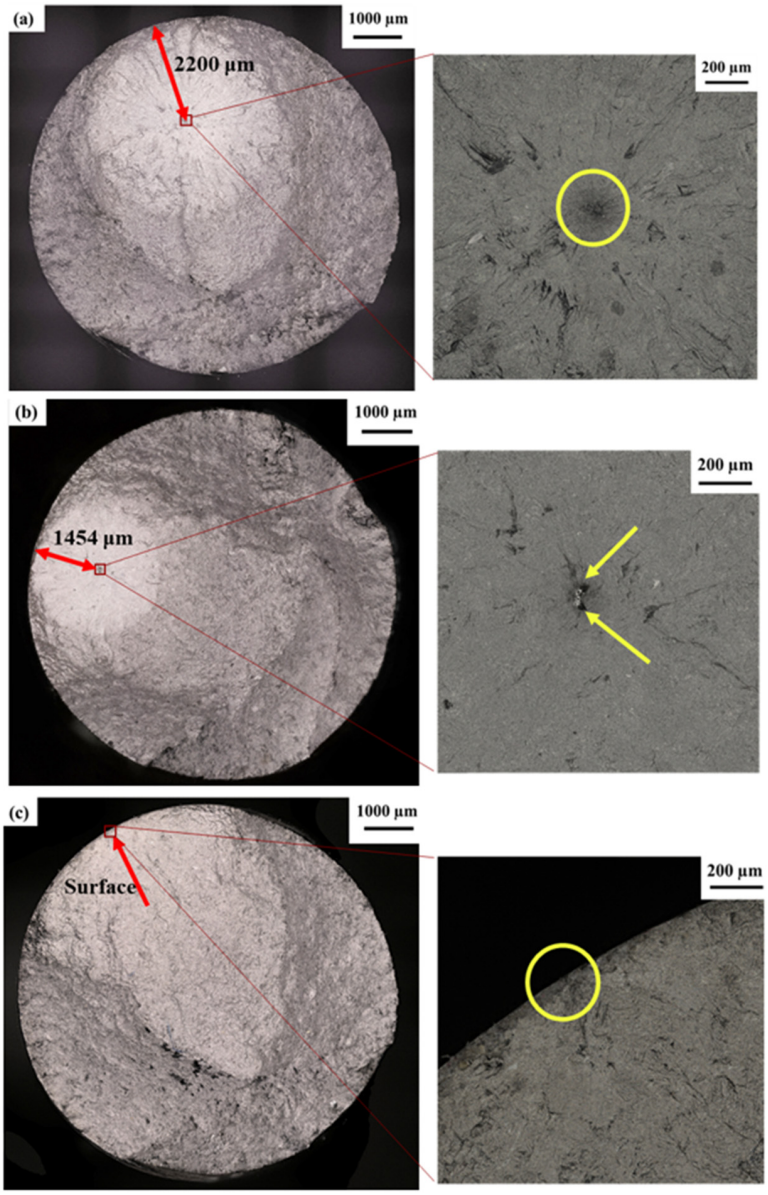

Figure 18. Fracture surface of three PBF1 non-LSP samples. (**a**,**b**) Interior initiation sites from 800 MPa maximum stress and (**c**) surface initiation site at 800 MPa maximum stress. The circles and arrows indicate the initiation sites in the magnified views.

While initiation location accounts for the difference in fatigue life for interior versus surface cracks, initial defect shape and size also play notable roles in the scatter of the fatigue results for PBF1 non-LSP samples at similar depths. Each defect has a stress concentration dependent on its geometry that can make the experienced stress higher at certain points. For example, Figure 18 also shows the magnified views of the corresponding initiation defects for the samples. The crack-initiating defect shown in part a has a rounded shape with no sharp corners or clear high concentration areas. On the other hand, part b has two sharp points of high concentration, indicated by the arrows. Because of these high stress concentration areas in part b, the experienced stress at those points is expected to be larger than the 800 MPa maximum applied stress. As a result, the specimen failed about 7×10^5 cycles sooner than the sample with less stress concentration in part a. Surface cracks like those in Figure 18c may also experience differences in stress concentration based on geometry. Sharper surface defects will have higher experienced stresses resulting in shorter fatigue lives than those with smaller rounder initial defects.

The randomness of initiation locations and defects is maintained in PBF1 samples after LSP, as demonstrated by Figure 16, where both LSP and non-LSP initiation sites extend to depths greater that 2000 µm. For a more detailed discussion of PBF1 LSP data in Figure 16, the fracture surfaces and initiation sites for two PBF1 LSP samples under 700 MPa max stress that initiated from below the surface are shown Figure 19. The initiation sites differ in depth by 1550 µm under the same applied maximum stress of 700 MPa. Furthermore, there are differences in defect geometry with more prominent stress concentrations for the sample shown in Figure 19a highlighted by the arrows. With these patterns matching those of samples not exposed to LSP, it implies that the scatter in crack initiation is still present after LSP, as also shown in Figure 16. Despite the randomness in defect initiation sites, the LSP samples have added residual stresses that impact the uniformity of the experienced stress, and in turn the fatigue lives.

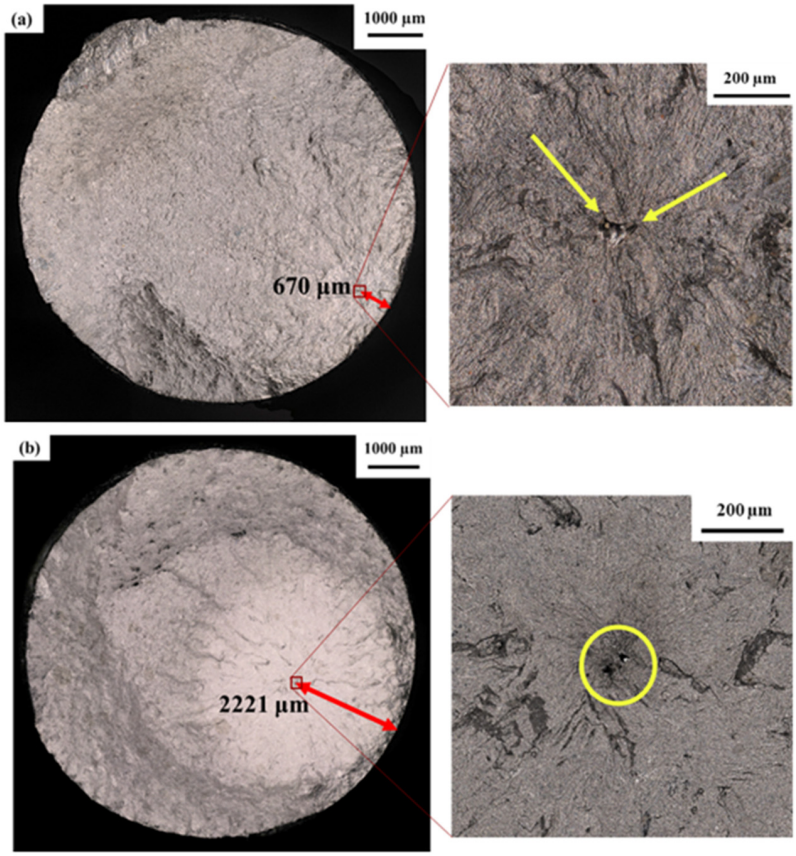

Figure 19. (**a**,**b**) Fracture surfaces of PBF1 LSP samples under 700 MPa. The circles and arrows indicate the interior initiation sites in the magnified views.

As shown in Figure 13, compressive residual stresses near the surface are between −225 MPa and −574 MPa at a depth up to 17 µm for PBF1 samples after LSP. The compressive residual stress gradually decreases as the distance from the surface increases, and ultimately transitions to tensile residual stress at approximately 300 µm below the surface for the machined samples. This means that defects near the surface are experiencing less stress than what is applied, while the interior defects experience more stress. The effect can be coupled with the fact that the interior crack initiation samples typically have a longer fatigue life than surface initiation samples under the same stress. The shorter life surface initiations seem to lengthen due to the compressive residual stress and lower experienced stress. As illustrated in Figure 16, the samples that resulted in the shortest life for both LSP and non-LSP at 800 MPa maximum stress had cracks initiate from the surface. At this stress level, the shortest life was 35,056 cycles without LSP. After LSP, the shortest life at the same

stress level more than doubled to a value of 95,386 cycles. Because the compressive residual stresses lowered what was experienced at the surface by about 225 MPa, the fatigue life clearly improved under the same applied load.

The way LSP affected the life of interior cracks is most noticeable when comparing the interior crack initiations between different stress levels. It is expected that higher applied stress would result in a shorter fatigue life, and conversely, lower applied stress would result in a longer fatigue life. However, the fatigue life of LSP samples with interior crack initiations subjected to a stress amplitude of 700 MPa is roughly equal to that of non-LSP samples subjected to 800 MPa with interior crack initiations as can be seen in Figure 16. This lack of improvement in fatigue life despite the lower applied stress is likely a result of the tensile residual stresses present at depths greater than 300 µm in solid rod samples after LSP. The tensile residual stresses increased the experienced stress for interior initiations subjected to LSP, and in turn, caused a noticeable decrease in expected fatigue life. Because interior crack initiation failures typically have longer lives, the application of LSP and internal tensile residual stresses shorten what would be the longer end of the fatigue life range. This acts in parallel with the compressive residual stresses at the surface, which lengthen the lives of the surface initiation failures. Ultimately, the combination of residual stresses caused by LSP reduce the gap between the short-life surface failures and long-life interior failures to reduce the presence of scatter in the fatigue lives of LSP samples.

Conversely to the trend of PBF1, PBF2 samples demonstrated limited scatter for both the non-LSP and LSP tests, along with an improved fatigue life for the PBF2 LSP samples, as shown in Figure 15. The differences in defect characteristics and locations between PBF1 and PBF2 likely contribute to the varying trends of LSP's effect on fatigue behavior. The images of the polished cross sections for solid rod PBF1 and PBF2 samples are shown in Figure 20. The estimated count for the PBF1 samples was 587 defects, accounting for approximately 0.4% of the cross-sectional area, while the number of defects for a single cross section of a PBF2 sample was estimated to be 2246, accounting for approximately 0.8% of the cross-sectional area. Figure 21 shows the distribution for the quantity of defects in specified size ranges, in terms of area. It is clear that PBF2 samples possess larger defects than PBF1, likely in the form of irregularly shaped lack of fusion defects.

The distribution of the crack initiation sites and effective areas with their corresponding fatigue lives for PBF2 samples is presented Figure 22. Because of the increased number and size of interior defects in PBF2, the effect of surface roughness is less impactful compared to PBF1. This resulted in a notable shift in the crack initiations to sub surface locations after LSP and consequently improved fatigue life for PBF2 samples. Figure 22 shows that all cracks initiated at depths not more than 200 µm below the surface and tend to cluster around 100–150 µm. This puts all LSP PBF2 samples well within the range of the compressive residual stressed area. The consistency in crack initiation sites likely contributes to the consistency in fatigue life for specimens of the same type, along with the noticeable improvement in fatigue after LSP. The internal tensile residual stress caused by LSP for the PBF2 LSP samples does not have the potential to increase the experienced stress and hinder the fatigue performance. Thus, the primary influence of LSP on PBF2 is the beneficial effects of compressive residual that can slow down the crack initiation and, ultimately fatigue failures.

4.4. Mean Stress Correction Modeling

Modeling was completed for machined specimens utilizing only the PBF2 data. PBF1 samples were not modeled because of the limited number of stress levels used during fatigue testing. Table 6 presents the data for initiation depth, compressive residual stress at that depth, and the corrected stresses for each sample. As discussed in Section 3.4, the SWT mean stress correction model shows strong results for Ti-6Al-4V material and resulted in a good correlation between the non-LSP and LSP data of the as-built samples. Because of this, SWT was selected as the first model used for the PBF2 machined data. Figure 23a,b show the fatigue data and the corresponding SWT parameter vs. life plot, respectively. Unlike

the as-built data, the SWT model does not do as well with correlating the non-LSP and LSP results for the machined specimens, where most of the LSP data falls near or outside of the 3× scatter bands.

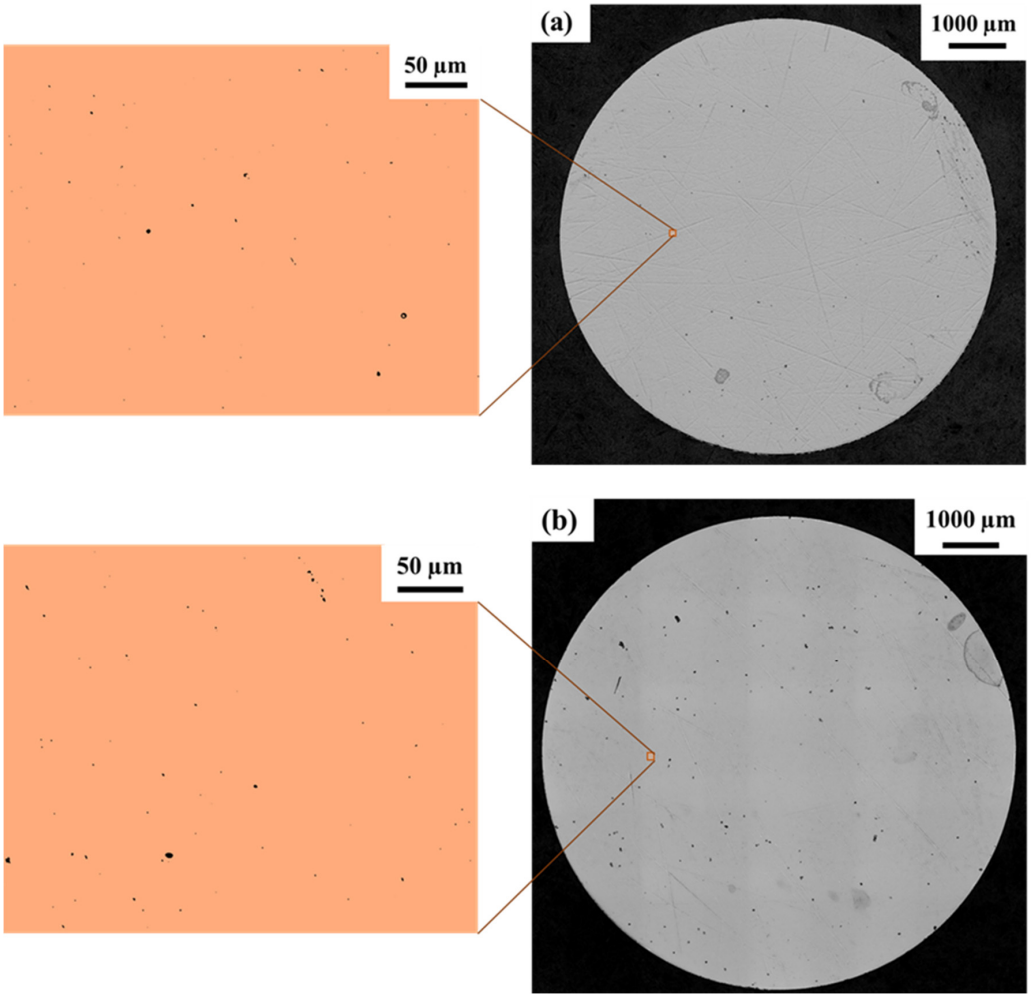

Figure 20. Defect images for (**a**) PBF1 and (**b**) PBF2 process parameters with magnified areas.

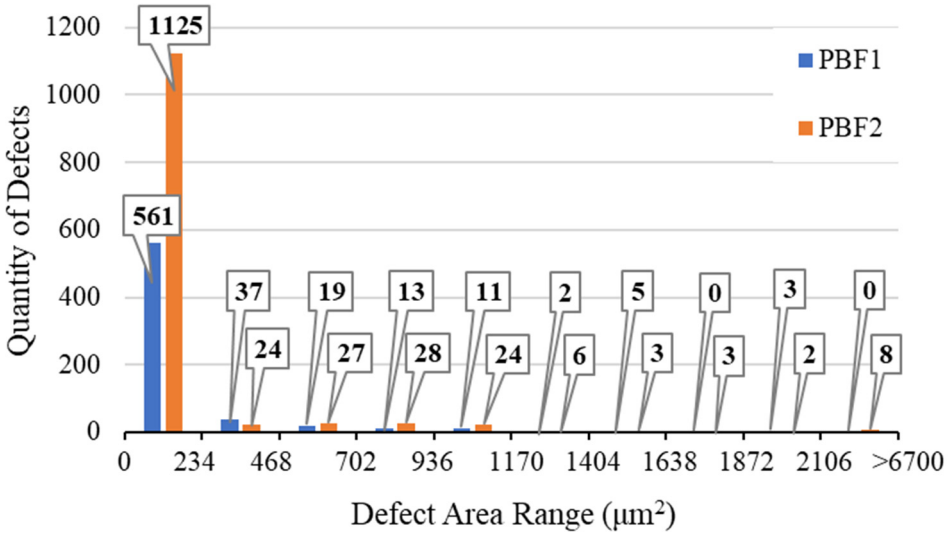

Figure 21. Defect size distribution for PBF1 and PBF2 machined specimens.

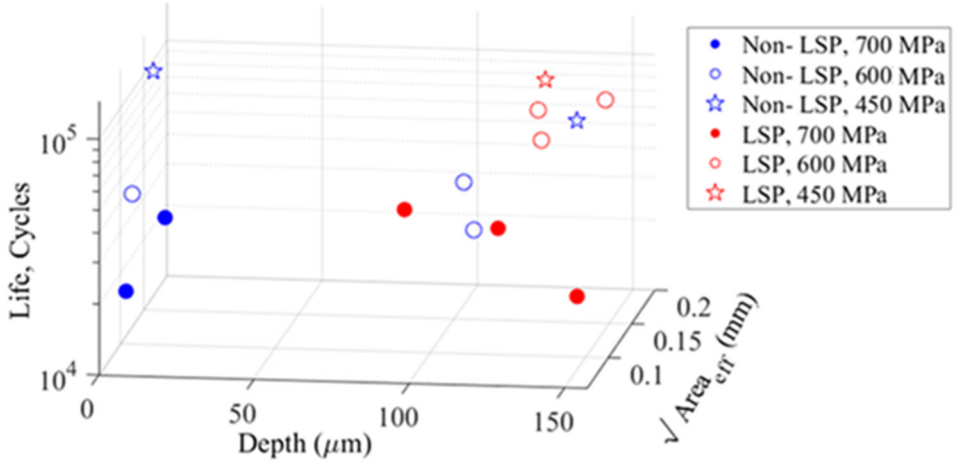

Figure 22. Life, crack-initiating defect depth, and defect effective area for non-optimized PBF2 uniaxial samples.

Table 6. Summary of defect depth, corrected stresses, and life for PBF2 samples with machined surface.

	Depth (μm)	Residual Stress (MPa)	Nominal Max Stress (MPa)	Corrected Max Stress (MPa)	Corrected Mean Stress (MPa)	N_f (Cycles)	R Ratio
Non-LSP	-	0	700	700	385	15,434	0.1
	-	0	700	700	385	16,549	0.1
	-	0	600	600	330	36,635	0.1
	-	0	600	600	330	30,855	0.1
	-	0	450	450	225	114,375	0.1
	-	0	450	450	225	90,221	0.1
	-	0	600	600	330	34,735	0.1
	-	0	700	700	385	18,309	0.1
LSP	154	−260	700	440	125	24,589	−0.43
	129	−325	450	125	−77.5	102,460	−2.24
	141	−280	600	320	50	145,000	−0.69
	157	−212	600	388	118	129,545	−0.39
	118	−380	700	320	5	29,005	−0.97
	128	−325	600	275	5	58,449	−0.96
	92	−480	700	220	−95	40,946	−1.86

Surface condition is the primary factor that may have influenced the effectiveness of the SWT model for machined specimens. A previous study by Fatemi et al. [38] discussed the effect of varying surface post processing on material behavior under cyclic loading. It was stated that surface machining can increase the ductility of a component which results in different fatigue behavior compared to the brittle behavior of as-built surface components. The increased ductility shifts the failure mode of the material from tensile (i.e., brittle behavior) to shear (i.e., ductile behavior). Because the SWT method is primarily used for brittle-behaving materials, the shift to shear failure mechanism and ductile-behaving after machining likely impacted the accuracy of the SWT model. Consequently, a different method that can account for the shear nature of ductile failures is needed to appropriately model the machined surface data.

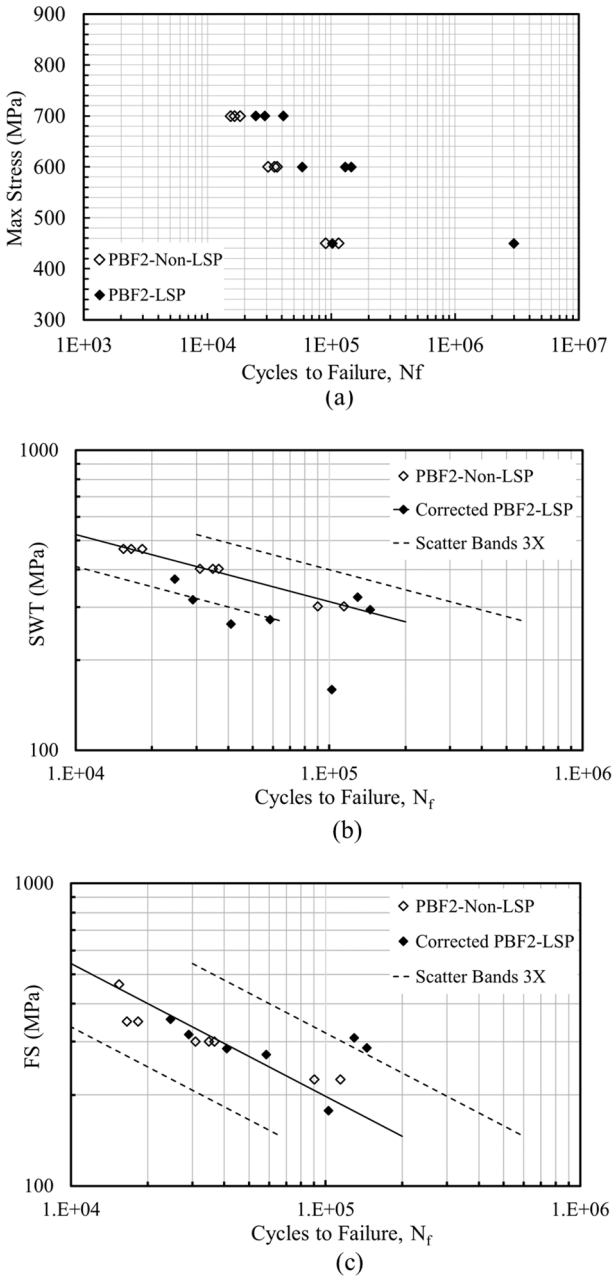

Figure 23. (**a**) Axial loading fatigue test results for PBF2 solid rod samples, and mean stress corrected results using (**b**) SWT and (**c**) FS models. FS results in better data correlations for the majority of the data.

One of the most common parameters used to model fatigue behavior under a shear-based failure mechanism is the Fatemi-Socie (FS) fatigue damage parameter shown in Equation (3) [39].

$$FS = \frac{\Delta\gamma_{max}}{2}\left(1 + k\frac{\sigma_{n,max}}{\sigma_y}\right) \quad (3)$$

However, in 2016 a modified form of this parameter was presented by Gate and Fatemi, and is shown in Equation (4), where $\Delta\gamma$ is the shear strain range on the plane that experiences the maximum shear strain range, $\Delta\gamma_{max}$ is the maximum shear strain range experienced on the plane where the damage parameter is maximized, $\sigma_{n,max}$ is the maximum normal stress occurring on the plane that the $\Delta\gamma_{max}$ occurs, G is the shear

modulus, and k is the material-dependent parameter reflecting the effect of normal stress on fatigue damage [40].

$$FS = \frac{\Delta\gamma_{max}}{2}\left(1 + k\frac{\sigma_{n,max}}{G\Delta\gamma}\right) \quad (4)$$

The modified parameter is very similar to the original FS parameter but is said to better account for an applied mean tensile stress. As a result, the Gates and Fatemi modified FS-parameter was selected as the second modeling method of the machined surface data. Figure 23c presents the modified FS parameter vs. life plot for the PBF2 machined surface data. As can be seen, there is a much stronger correlation between the non-LSP and LSP data compared to the SWT results in part b, where the majority of LSP data is located within the 3× scatter band of the non-LSP S-N line. This indicates that, for machined surfaces, the modified FS parameter can effectively estimate the fatigue behavior of LSP components with known residual stresses using non-LSP data.

5. Conclusions

This paper discussed the effect of LSP on surface roughness and the fatigue properties of Ti-6Al-4V structures fabricated through Powder Bed Fusion. LSP uses a plasma induced shock wave to cause slight plastic deformation near the surface of a component. This process affects the surface condition of the component, experienced stress, and the resulting fatigue strength. Based on the experimental results and analyses presented, the following conclusions can be drawn:

- Part geometry plays an important role when subjected to LSP. It was observed that for the same LSP process parameters, the geometry with partial target area results in more compressive residual stresses near the surface, which are thought to be caused by equilibrium satisfaction.
- Some roughness measurement techniques may not be useful for the AM as-built surface components. While the mechanical profilometer did not show any roughness changes after the LSP process on the as-built surface specimens, a destructive approach was employed, indicating significant changes. This was discussed to be due to the limitations of the mechanical profilometer in reaching the deep valleys of the profile.
- When no opaque layer is used, it was observed that the LSP process results in notable improvements in the surface profile of as-built samples by removing the loosely bounded unmelted particles and reflowing the material at sharp valleys. Unlike the as-built surface roughness improvements after LSP, the roughness of the machined surface specimens increases because of the laser waves.
- It was observed that the LSP process does not improve the fatigue lives when optimized process parameters are used for part fabrication and the surface is machined. This was found to be due to the contradicting effects of compressive residual stresses near the surface and the worsened roughness due to the LSP process. However, while there was not a clear improvement in their fatigue strength, a notable decrease in the scatter was observed for the optimized samples with machined surface conditions.
- While the fatigue behavior of optimized machined samples did not necessarily improve after LSP, the non-optimized samples showed significant improvements in fatigue lives along with decreased scatters. This was found to be due to the defect quantity and distributions in these samples which generate more consistency and repeatability in the potential for the cracks to initiate at or near the surface for both non-LSP and LSP samples.
- When the surface condition is as-built, LSP significantly improves the fatigue lives regardless of the AM process parameters (i.e., optimized vs. non-optimized). This is due to the improved surface profiles of these samples after the LSP process, which reduces the stress concentration effects of the rough surface by healing the sharp valleys and removing the loosely bounded particles at the surface.
- It was observed that although the SWT criterion correlated the fatigue test results of the LSP and non-LSP with as-built surfaces reasonably well, it was not able to correlate the data with machined surfaces.

- Using the Fatemi-Socie parameter for the machined surface condition resulted in good data correlations. This parameter is based on shear damage and has recently been found to work for material with a transition from shear to tensile stresses [41]. This worked well for the shear damage mechanism of the AM Ti-6Al-4V alloy with a machined surface.

As advancements are made in AM technologies, there is the potential for additional studies related to LSP and the fatigue properties of AM materials. One area for future work is the effect of localized LSP for notches and stress concentrations. LSP is limited by part size, so applying LSP in only small stress concentration areas could still provide the benefits of LSP for a larger component despite its size. Another area for continued research is LSP and multiaxial fatigue loadings. Most loadings are complex and not limited to one axis. Thus, it is important to also understand how components subjected to LSP may react under these stress conditions. Lastly, numerous parameters and conditions influence the effectiveness and impact of LSP. Generating numerical modeling and predictive methods that incorporate part size, AM and LSP process parameters could have vast contributions to the field.

Author Contributions: Conceptualization, K.D., S.Z., D.R., E.A. and R.M.; Methodology, K.D., S.G., S.Z., D.R., E.A. and R.M.; Software, S.G.; Validation, R.M.; Formal analysis, K.D. and S.G.; Investigation, K.D., S.G., S.Z., D.R., E.A. and R.M.; Resources, S.Z., D.R., E.A. and R.M.; Data curation, K.D., S.G. and R.M.; Writing—original draft, K.D. and S.G.; Writing—review & editing, K.D., S.G., S.Z., D.R., E.A. and R.M.; Visualization, K.D. and S.G.; Supervision, E.A. and R.M.; Project administration, E.A. and R.M.; Funding acquisition, E.A. and R.M. All authors have read and agreed to the published version of the manuscript.

Funding: This research received no external funding.

Institutional Review Board Statement: Not applicable.

Informed Consent Statement: Not applicable.

Data Availability Statement: Data are contained within the article.

Acknowledgments: The authors would like to thank Michael Fitzmire of Boeing (Formerly Graduate Student at Mechanical Engineering Department of The University of Memphis) for fabricating the AM parts and helping with the LSP applications to the samples.

Conflicts of Interest: Author Ebrahim Asadi was employed by the company Medtronic Plc. The remaining authors declare that the research was conducted in the absence of any commercial or financial relationships that could be construed as a potential conflict of interest.

Nomenclature

E	Energy Density
h	Hatch Spacing
G	Shear Modulus
K	FS Material Dependent Constant
N_f	Cycles to Failure
P	Laser Power
R_a	Arithmetic Mean of Surface Roughness
R_v	Maximum Profile Valley Depth
R_t	Total Height of Roughness Profile
R_z	Maximum Height of Roughness Profile
S_e	Equivalent Stress
t	Layer Thickness
v	Laser Scan Speed
$\Delta\gamma_{max}$	Maximum Shear Strain Range
σ_a	Axial Stress Amplitude
σ_{max}	Max Applied Stress
$\sigma_{n,max}$	Maximum Normal Stress on Maximum Shear Plane
$\sqrt{area_{eff}}$	Effective Crack Initiation Area

Abbreviations

AB	As-Built Surface
AM	Additive Manufacturing/Additive Manufactured
DED	Directed Energy Deposition
E-PBF	Electron Beam Powder Bed Fusion
FS	Fatemi-Socie
LOF	Lack of Fusion
L-PBF	Laser Powder Bed Fusion
LSP	Laser Shock Peening
M	Machined Surface
OM	Optical Microscope
PBF	Powder Bed Fusion
SWT	Smith-Watson-Topper

References

1. Fatemi, A.; Molaei, R.; Sharifimehr, S.; Phan, N.; Shamsaei, N. Multiaxial fatigue behavior of wrought and additive manufactured Ti-6Al-4V including surface finish effect. *Int. J. Fatigue* **2017**, *100*, 347–366. [CrossRef]
2. Fatemi, A.; Molaei, R.; Simsiriwong, J.; Sanaei, N.; Pegues, J.; Torries, B.; Phan, N.; Shamsaei, N. Fatigue behaviour of additive manufactured materials: An overview of some recent experimental studies on Ti-6Al-4V considering various processing and loading direction effects. *Fatigue Fract. Eng. Mater. Struct.* **2019**, *42*, 991–1009. [CrossRef]
3. Kumar, R.; Kumar, M.; Chohan, J.S. The role of additive manufacturing for biomedical applications: A critical review. *J. Manuf. Process.* **2021**, *64*, 828–850. [CrossRef]
4. Fatemi, A.; Molaei, R.; Sharifimehr, S.; Shamsaei, N.; Phan, N. Torsional fatigue behavior of wrought and additive manufactured Ti-6Al-4V by powder bed fusion including surface finish effect. *Int. J. Fatigue* **2017**, *99*, 187–201. [CrossRef]
5. Pegues, J.; Shao, S.; Shamsaei, N.; Sanaei, N.; Fatemi, A.; Warner, D.; Li, P.; Phan, N. Fatigue of additive manufactured Ti-6Al-4V, Part I: The effects of powder feedstock, manufacturing, and post-process conditions on the resulting microstructure and defects. *Int. J. Fatigue* **2020**, *132*, 105358. [CrossRef]
6. Sanaei, N.; Fatemi, A.; Phan, N. Defect characteristics and analysis of their variability in metal L-PBF additive manufacturing. *Mater. Des.* **2019**, *182*, 108091. [CrossRef]
7. Oliveira, J.P.; LaLonde, A.D.; Ma, J. Processing parameters in laser powder bed fusion metal additive manufacturing. *Mater. Des.* **2020**, *193*, 108762. [CrossRef]
8. Renzo, D.A.; Maletta, C.; Sgambitterra, E.; Furgiuele, F.; Berto, F. Surface roughness effect on multiaxial fatigue behavior of additively manufactured Ti6Al4V alloy. *Int. J. Fatigue* **2022**, *163*, 107022. [CrossRef]
9. Taufik, M.; Jain, P.K. Role of build orientation in layered manufacturing: A review. *Int. J. Manuf. Technol. Manag.* **2013**, *27*, 47–73. [CrossRef]
10. Jafari, D.; Wits, W.W. The utilization of selective laser melting technology on heat transfer devices for thermal energy conversion applications: A review. *Renew. Sustain. Energy Rev.* **2018**, *91*, 420–442. [CrossRef]
11. Ulbricht, A.; Altenburg, S.J.; Sprengel, M.; Sommer, K.; Mohr, G.; Fritsch, T.; Mishurova, T.; Serrano-Munoz, I.; Evans, A.; Hofmann, M.; et al. Separation of the formation mechanisms of residual stresses in lpbf 316l. *Metals* **2020**, *10*, 1234. [CrossRef]
12. Stephens, R.I.; Fatemi, A.; Stephens, R.R.; Fuchs, H.O. *Metal Fatigue in Engineering*; Wiley: Hoboken, NJ, USA, 2001.
13. Gujba, A.K.; Medraj, M. Laser peening process and its impact on materials properties in comparison with shot peening and ultrasonic impact peening. *Materials* **2014**, *7*, 7925–7974. [CrossRef] [PubMed]
14. Li, W.; Huang, H.; Xu, D.; Chen, J.; Zuo, L.; Ma, G.; He, J.; Li, C.; Peng, Z.; Ren, Y.; et al. Effect of Laser Shock Processing and Aluminizing on Microstructure and High-Temperature Creep Properties of 321 Stainless Steel for Solar Thermal Power Generation. *Int. J. Photoenergy* **2020**, *2020*, 6532820. [CrossRef]
15. Pathak, S.; Zulić, S.; Kaufman, J.; Kopeček, J.; Stránský, O.; Böhm, M.; Brajer, J.; Beránek, L.; Shukla, A.; Ackermann, M.; et al. Post-processing of selective laser melting manufactured SS-304L by laser shock peening. *J. Mater. Res. Technol.* **2022**, *19*, 4787–4792. [CrossRef]
16. Deng, W.W.; Lu, H.F.; Xing, Y.H.; Luo, K.Y.; Lu, J.Z. Effect of laser shock peening on tensile properties and microstructure of selective laser melted 316L stainless steel with different build directions. *Mater. Sci. Eng. A* **2022**, *850*, 143567. [CrossRef]
17. Aguado-Montero, S.; Navarro, C.; Vázquez, J.; Lasagni, F.; Slawik, S.; Domínguez, J. Fatigue behaviour of PBF additive manufactured TI6AL4V alloy after shot and laser peening. *Int. J. Fatigue* **2022**, *154*, 106536. [CrossRef]
18. Luo, S.; He, W.; Chen, K.; Nie, X.; Zhou, L.; Li, Y. Regain the fatigue strength of laser additive manufactured Ti alloy via laser shock peening. *J. Alloys Compd.* **2018**, *750*, 626–635. [CrossRef]
19. Yang, K.; Huang, Q.; Zhong, B.; Wang, Q.; Chen, Q.; Chen, Y.; Su, N.; Liu, H. Enhanced extra-long life fatigue resistance of a bimodal titanium alloy by laser shock peening. *Int. J. Fatigue* **2020**, *141*, 105868. [CrossRef]

20. Leuders, S.; Thöne, M.; Riemer, A.; Niendorf, T.; Tröster, T.; Richard, H.; Maier, H. On the mechanical behaviour of titanium alloy TiAl6V4 manufactured by selective laser melting: Fatigue resistance and crack growth performance. *Int. J. Fatigue* **2013**, *48*, 300–307. [CrossRef]
21. Zhang, J.; Fatemi, A. Surface roughness effect on multiaxial fatigue behavior of additive manufactured metals and its modeling. *Theor. Appl. Fract. Mech.* **2019**, *103*, 102260. [CrossRef]
22. Molaei, R.; Fatemi, A.; Phan, N. Multiaxial fatigue of LB-PBF additive manufactured 17-4 PH stainless steel including the effects of surface roughness and HIP treatment and comparisons with the wrought alloy. *Int. J. Fatigue* **2020**, *137*, 105646. [CrossRef]
23. *ASTM standard E466*; Standard Practice for Conducting Force Controlled Constant Amplitude Axial Fatigue Tests of Metallic Materials. ASTM: West Conshohocken, PA, USA, 2021.
24. Bjerregaard, L. *Metalog Guide*; Struers: Ballerup, Denmark, 2000.
25. Maleki, E.; Bagherifard, S.; Bandini, M.; Guagliano, M. Surface post-treatments for metal additive manufacturing: Progress, challenges, and opportunities. *Addit. Manuf.* **2021**, *37*, 101619. [CrossRef]
26. Nicoletto, G. Directional and notch effects on the fatigue behavior of as-built DMLS Ti6Al4V. *Int. J. Fatigue* **2018**, *106*, 124–131. [CrossRef]
27. Solberg, K.; Berto, F. A diagram for capturing and predicting failure locations in notch geometries produced by additive manufacturing. *Int. J. Fatigue* **2020**, *134*, 105428. [CrossRef]
28. Thorslund, T.; Kahlen, F.J.; Kar, A. Temperatures, pressures and stresses during laser shock processing. *Opt. Lasers Eng.* **2003**, *39*, 51–71. [CrossRef]
29. Fabbro, R.; Peyre, P.; Berthe, L.; Sollier, A.; Bartnicki, E. Physics and Applications of Laser Shock Processing of Materials. *High-Power Lasers Manuf.* **2000**, *3888*, 155–164.
30. Gupta, R.K.; Pant, B.K.; Kain, V.; Kaul, R.; Bindra, K.S. Laser Shock Peening and its Applications: A Review. *Lasers Manuf. Mater. Process.* **2019**, *6*, 424–463. [CrossRef]
31. Yadav, M.J.; Jinoop, A.N.; Danduk, C.; Subbu, S.K. Laser Shock Processing: Process Physics, Parameters, and Applications. *Mater. Today Proc.* **2017**, *4*, 7921–7930. [CrossRef]
32. Shen, X.; Shukla, P.; Nath, S.; Lawrence, J. Improvement in mechanical properties of titanium alloy (Ti-6Al-7Nb) subject to multiple laser shock peening. *Surf. Coat. Technol.* **2017**, *327*, 101–109. [CrossRef]
33. Derrick, C.; Fatemi, A. Correlations of fatigue strength of additively manufactured metals with hardness and defect size. *Int. J. Fatigue* **2022**, *162*, 106920. [CrossRef]
34. Smith, K.; Watson, P.; Topper, T. Stress-strain function for the fatigue of metals. *J. Mater.* **1970**, *5*, 767–778.
35. Nasab, M.H.; Vedani, M.; Logé, R.E.; Sohrabi, N.; Jamili, A.M.; du Plessis, A.; Beretta, S. An investigation on the fatigue behavior of additively manufactured laser shock peened AlSi7Mg alloy surfaces. *Mater. Charact.* **2023**, *200*, 112907. [CrossRef]
36. Yamashita, Y.; Murakami, T.; Mihara, R.; Okada, M.; Murakami, Y. Defect Analysis and Fatigue Design Basis for Ni-based Superalloy 718 manufactured by Additive Manufacturing. In *Procedia Structural Integrity*; Elsevier B.V.: Amsterdam, The Netherlands, 2017; pp. 11–18. [CrossRef]
37. Murakami, Y.; Kodama, S.; Konuma, S. Quantitative evaluation of effects of non-metallic inclusions on fatigue strength of high strength steels. I: Basic fatigue mechanism and evaluation of correlation between the fatigue fracture stress and the size and location of non-metallic inclusions. *Int. J. Fatigue* **1989**, *1*, 291–298. [CrossRef]
38. Fatemi, A.; Molaei, R.; Phan, N. Multiaxial fatigue of additive manufactured metals: Performance, analysis, and applications. *Int. J. Fatigue* **2020**, *134*, 105479. [CrossRef]
39. Fatemi, A.; Socie, D.F. A critical plane approach to multiaxial fatigue damage including out-of-phase loading. *Fatigue Fract. Eng. Mater. Struct.* **1988**, *11*, 149–165. [CrossRef]
40. Gates, N.R.; Fatemi, A. On the consideration of normal and shear stress interaction in multiaxial fatigue damage analysis. *Int. J. Fatigue* **2017**, *100*, 322–336. [CrossRef]
41. Molaei, R.; Fatemi, A. On the transition from shear to tensile failure mode in multiaxial fatigue. *Int. J. Fatigue* **2024**, *180*, 108076. [CrossRef]